As Predicted and More: Modulated Channel Occupation in YZn_{5+x}

Authors

Rie T. Fredrickson^{a*} and Daniel C. Fredrickson^{a*}

^aDepartment of Chemistry, University of Wisconsin-Madison, 1101 University Avenue, Madison, WI, 53706, United States

Correspondence email: rie.fredrickson@wisc.edu; danny@chem.wisc.edu

Funding information National Science Foundation, Directorate for Mathematical and Physical Sciences (grant No. DMR-2127349).

Synopsis We use the superspace approach to determine the structure of a modulated form of YZn_{5+x} (x=0.217), which is an ordered variant of the previously described $EuMg_{5+x}$ -type structure, with its channels containing disordered Zn atoms. The details of the pattern align closely with earlier predictions based on DFT-Chemical Pressure analysis of ordered models.

Like many complex intermetallic phases, the crystal structures of REZn_{5+x} compounds (RE = lanthanide or group 3 element) based on the EuMg₅ type have gradually unfolded. The original reports described a complex hexagonal structure with an unusual combination of tetrahedrally closepacked regions and open spaces, as well as observations of superstructure reflections. More recently, we reinvestigated the structure of YZn₅, reclassifying it as the EuMg_{5+x}-type compound YZn_{5+x} ($x\approx0.2$), in which disordered channels run along c through the spaces formerly considered open. In addition, DFT-Chemical Pressure (DFT-CP) analysis of ordered models of YZn_{5+x} highlighted paths for communication between neighboring channels setting the stage for superstructure formation. Herein, we present the experimental elucidation of this effect with the synthesis and structure determination of a modulated form of YZn_{5+x} . By slow-cooling samples of YZn_{5+x} from the annealing temperature, crystals were obtained that exhibit satellite reflections with the modulation wave vector $\mathbf{q} = \frac{1}{3}\mathbf{a}^* + \frac{1}{3}\mathbf{b}^*$ + 0.3041**c***. Structure solution and refinement using a (3+1)D model in superspace group $P\bar{3}1c(\frac{1}{3}\frac{1}{3}\sigma_3)00s$ reveals incommensurate order in the structure's channels. Here, two Zn sites associated with channels are present, each with discontinuous atomic domains that are slanted in the x_3 x_4 plane. Their slanting corresponds to adjustments along the **c**-axis for the presence or absence of close neighbors along that axis, while the occupation patterns of neighboring channels are shifted by ½ of the modulation period. These features follow earlier predictions from CP analysis, highlighting how this approach can be used predictively in search of new phenomena.

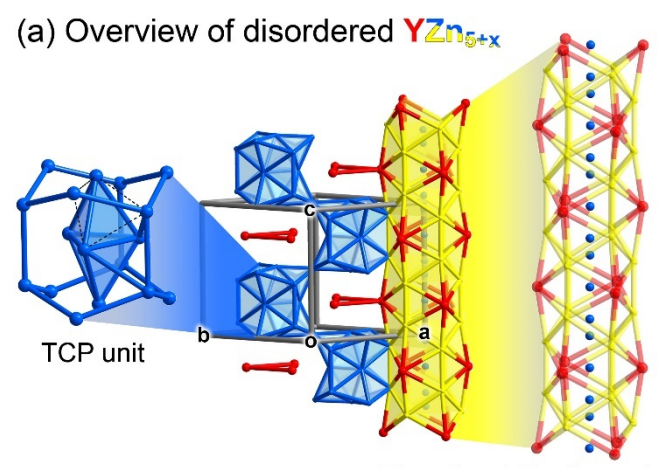
Keywords: Aperiodic crystals; crystal structure prediction; intermetallic phases

1. Introduction

When encountering disorder in a newly solved crystal structure, one faces several questions. Could an ordered superstructure be obtainable at different conditions or through variations in the crystallization or synthesis methods (Etzkorn et al., 2007, Lidin et al., 2009, Okamoto et al., 2017, Becker & Leineweber, 2018)? Or may a superstructure be present, but obscured by the balanced twinning of domains related by pseudosymmetry (Feuerbacher et al., 2007)? Does the randomness suggested by the crystallographic model belie local order that is just not pronounced enough to be detectable as diffuse scattering in the data available (Frey, 1995, Larsson et al., 1996)? Together, such possibilities relate to the origins of the apparent disorder in frustration or near degeneracy (Keen & Goodwin, 2015), and the potential ways in which the occupancies or positions of atoms in one region of disorder impacts the preferences of others. Over the past ten years, the DFT-Chemical Pressure (CP) analysis (Hilleke & Fredrickson, 2018, Lu et al., 2021) has emerged as a theoretical approach to analyze these effects, as illustrated by its ability to reveal paths of soft atomic motion underlying the channellike structures of the Nowotny Chimney Ladders (Lu & Fredrickson, 2019) and Fe₂Al₅ (Vinokur et al., 2019), as well as the packing issues faced by the disordered polyhedra in the quasicrystal approximant CaCd₆ (Berns & Fredrickson, 2013) and Fe₁₄Pd₁₇Al₆₉ (Peterson et al., 2020). More recently, this approach has been applied in a predictive fashion, in which CP analysis on models of the disordered EuMg_{5+x}-type compound YZn_{5+x} ($x\approx0.2$) pointed to a potential superstructure (Fredrickson *et al.*, 2022), a proposal that we herein experimentally investigate.

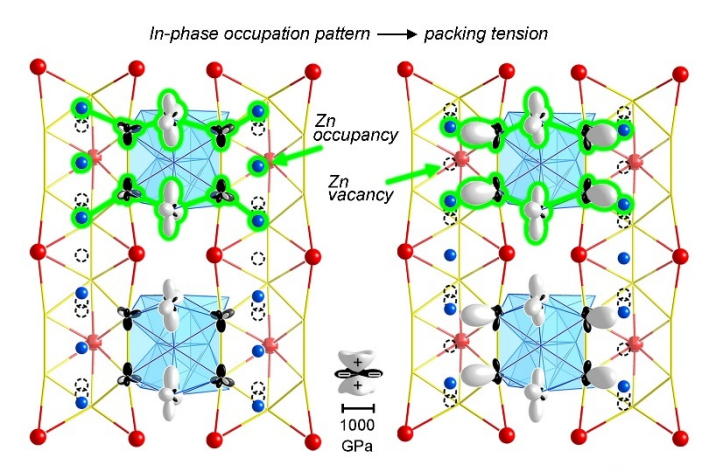
Several REZn₅ compounds (RE = lanthanide or group 3 transition metal) were originally reported by Fornasini and coworkers as adopting the EuMg₅ type (Mühlpfordt, 1970), with the observation that some crystals exhibited superstructure reflections corresponding to $\sqrt{3} \times \sqrt{3} \times 3$ or $\sqrt{3} \times \sqrt{3} \times 6$ supercells (Bruzzone et al., 1970, Fornasini, 1971). Intrigued by the structural relationship of these phases to the family of chemical pressure (CP)-driven variations of the CaCu₅ type (Berns & Fredrickson, 2014), as well as unusual open void spaces that appear in them, we recently reinvestigated the crystal structure of YZn₅ as a representative example (Fredrickson et al., 2022). Our structure solution revealed columns of disordered Zn atoms running along the hexagonal c axis (Figure 1a), placing this compound in the EuMg_{5+x} type (Erassme & Lueken, 1987, Mühlpfordt, 1997), a disordered variant of the EuMg₅ type adopted not only in RE-Mg and RE-Zn systems but also observed in Ni- and Al-based intermetallics (Gladyshevskii et al., 1993, Bohdana et al., 2020). While the X-ray diffraction patterns of these crystals showed no indication of a superstructure, DFT-CP analysis on a series of ordered models pointed to a mechanism for the occupation pattern of one channel to influence those of its surroundings (Figure 1b): Neighboring channels in the ab-plane are bridged through tetrahedrally-close-packed (TCP) units (blue), which are subject to different CP effects depending on whether the adjacent Zn sites in the channel are occupied or vacant. In both cases, the occupation or vacancy of the channel atom on both

sides of the TCP unit leads to an accumulation of stress, which could be relieved through a staggering of the occupation of neighboring columns. Based on this scheme, we proposed a superstructure pattern (Figure 1c) in which Zn atoms are distributed in an ordered fashion over two basic Zn positions along each channel to give rise to a tripling of the **c** repeat vector, with the patterns of neighboring channels being shifted relative to each other by 1 subcell.



Disordered Zn channel

(b) CP features between Zn channels through bridging TCP units



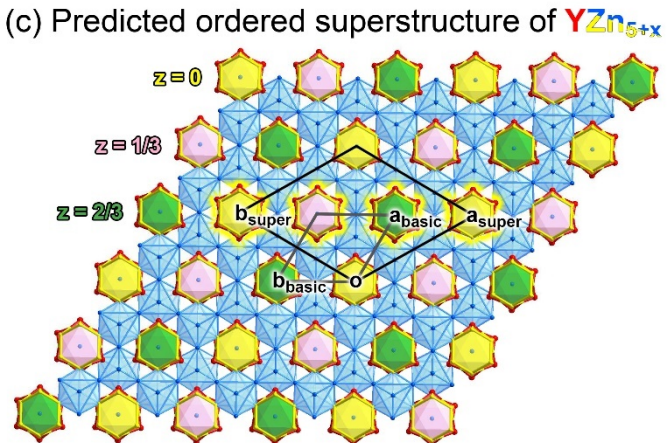


Figure 1 The disordered form of YZn_{5+x} ($x\approx0.2$) and its predicted superstructure from CP analysis. (a) The disordered YZn_{5+x} structure is constructed with tetrahedrally close packed (TCP) units, Y triangles, and Y-Zn channels (yellow/red) that contain disordered Zn atoms (blue). (b) Selected CP features calculated for ordered models of YZn_{5+x}, shown for points where neighboring Zn channels are bridged by TCP units, with the in-plane Zn positions in the channel being filled (left) or vacant (right). Black lobes correspond to directions of negative CP (where contraction is preferred), while white lobes indicate positive CP (where expansion of the structure would be favorable). (c) The $\sqrt{3}\times\sqrt{3}\times3$ superstructure predicted from the CP analysis, viewed down [001] with its basic cell outlined. Three colors are used for the channels to indicate the ½c_{super} shifts for the Zn occupation patterns between neighboring columns: yellow for $\Delta z=0$, pink for $\Delta z=\frac{1}{2}$, and green for $\Delta z=\frac{2}{3}$.

In this article, we experimentally demonstrate and elucidate the occurrence of channel ordering in YZn_{5+x}. Through a simple change in the temperature treatment in the synthetic procedure—allowing the reaction to slowly cool to ambient conditions from the annealing temperature (as opposed to quenching them in ice water)—crystals are obtained that exhibit both sharp diffraction peaks for the EuMg_{5+x}-type basic cell and additional reflections at intermediate points in reciprocal space. While the latter correspond approximately to the expected $\sqrt{3} \times \sqrt{3} \times 3$ supercell, their small number and relative weakness make solution as a conventional structure challenging. As we will see below, the structure solution and refinement proceed much more smoothly using the (3+1)D superspace approach (Janner & Janssen, 1980a, b, Smaalen, 2007), in which the additional reflections are indexed as satellites with **q**-vector $\mathbf{q} = \sigma_1 \mathbf{a}^* + \sigma_2 \mathbf{b}^* + \sigma_3 \mathbf{c}^* = \frac{1}{3} \mathbf{a}^* + \frac{1}{3} \mathbf{b}^* + 0.3041 \mathbf{c}^*$, and the structure is modeled as periodic in (3+1)D space with the additional dimension corresponding to the phase of a modulation function. The emerging crystal structure model confirms the general ordering pattern predicted by CP analysis, highlighting the predictive potential of CP-based models of structural effects.

2. Experimental Section

Synthesis. In our synthetic investigation of the Y-Zn system, elemental Y (Strem Chemicals, 99.9%) and Zn (Alfa Aesar, 99.9%) were used as starting materials. The elements were weighed out in the stoichiometric molar ratio of Y:Zn = 1:5 in an Ar-filled glove box, pressed into a pellet, and then placed into a fused silica tube, which was then evacuated and sealed. The sample was heated to 1100 °C for 24 hours to achieve a homogeneous melt, then annealed at 500 °C for 168 hours to allow for crystal growth, and finally cooled slowly to ambient temperature at a rate of 10 °C/hour.

Single Crystal X-ray Diffraction Analysis. Single crystal X-ray diffraction data for YZn_{5+x} (x=0.217) were collected on an Oxford Diffraction Xcalibur E diffractometer using graphite monochromatized Mo K α radiation (λ = 0.71073 Å) at ambient temperature. The collection and processing of the data set were performed using the CrysAlis Pro v.171.42.49 software supplied by the manufacturer. The structure was solved with the charge flipping algorithm (Oszlányi & Sütő, 2004,

2005, Palatinus, 2004) using the program SUPERFLIP (Palatinus & Chapuis, 2007) and refined on F^2 using the program JANA2006 (Petříček *et al.*, 2014). Further details regarding the refinements are given in Table 1 and the Supporting Information. The refined atomic coordinates and atomic displacement parameters for the average structure are given in Tables 2 and 3, respectively.

Table 1 Crystallographic Data for the Modulated Form YZn_{5+x}

<i>J</i> 8 1	5.%
Chemical formula	YZn _{5,217}
WDS composition	YZn _{5.26(3)}
a (Å), c (Å)	8.8811(1), 9.2057(1)
Volume (basic cell, Å ³)	628.812(12)
Z	6
Modulation wave vector ^a	$\mathbf{q} = \frac{1}{3}\mathbf{a} + \frac{1}{3}\mathbf{b} + 0.3041\mathbf{c} + 0.3041\mathbf{c}$
Superspace group	$P\overline{3}1c(\frac{1}{3}\frac{1}{3}\sigma_3)00s$
Symmetry operations	$(x_1, x_2, x_3, x_4), (-x_2, x_1-x_2, x_3, -x_2+x_4),$
	$(-x_1+x_2, -x_1, x_3, -x_1+x_4), (-x_2, -x_1, -x_3+\frac{1}{2}, -x_4+\frac{1}{2}),$
	$(-x_1+x_2, x_2, -x_3+1/2, x_2-x_4+1/2),$
	$(x_1, x_1-x_2, -x_3+\frac{1}{2}, x_1-x_4+\frac{1}{2}),$
	$(x_2, -x_1+x_2, -x_3, x_2-x_4), (x_1-x_2, x_1, -x_3, x_1-x_4),$
	$(x_2, x_1, x_3+\frac{1}{2}, x_4+\frac{1}{2}), (x_1-x_2, -x_2, x_3+\frac{1}{2}, -x_2+x_4+\frac{1}{2}),$
	$(-x_1, -x_1+x_2, x_3+1/2, -x_1+x_4+1/2), (-x_1, -x_2, -x_3, -x_4)$
Crystal dimensions (mm³)	$0.193 \times 0.137 \times 0.092$
Crystal color, habit	Metallic grey, prismatic
Data collection temperature	Ambient
Radiation source, λ (Å)	Mo K α sealed tube, 0.71073
Absorption correction	Analytical
Min/max transmission	0.024/0.125
$ heta_{ m min}, heta_{ m max}$	3.27/27.87
Refinement method	F^2
Number of reflections	24910
Unique refl. $[I > 3\sigma(I), all]$	777, 1450
$R_{int}[I > 3\sigma(I), all]$	5.24, 5.55
Number of parameters, constraints	90, 0
overall reflections	
$R[I > 3\sigma(I)], R_w[I > 3\sigma(I)]$	2.72, 7.88
R(all), R _w (all)	5.60, 8.76
$S[I > 3\sigma(I)], S(all)$	1.94, 1.53
main reflections	
$R[I > 3\sigma(I)], R_w[I > 3\sigma(I)]$	1.76, 6.58
R(all), R _w (all)	1.90, 6.63
satellite reflections	
$R[I > 3\sigma(I)], R_w[I > 3\sigma(I)]$	11.12, 18.87

R(all), R _w (all)	24.85, 23.72
$\Delta \rho_{\text{max}}, \Delta \rho_{\text{min}}(\text{electrons/Å}^3)$	4.73/-4.90

^aRefined **q**-vector without symmetry-constraints: $\mathbf{q} = 0.3337(6)\mathbf{a}^* + 0.3314(6)\mathbf{b}^* + 0.3041(7)\mathbf{c}^*$

Table 2 Refined atomic coordinates for the basic structure of YZn_{5+x} .

Site	Multiplicity	x	у	Z	U_{equiv}	Occupancy
Y	6	0.61475(10)	0.80738(5)	1/4	0.0107(3)	1
Znl	6	0.86508(10)	0.43254(5)	1/4	0.0117(3)	1
Zn2	4	2/3	1/3	0.51174(10)	0.0122(3)	1
Zn3	6	1	1/2	1/2	0.0123(6)	1
Zn4	12	0.8383(2)	0.67858(8)	0.41030(6)	0.0139(5)	1
Zn5	2	1	1	0	0.0196(12)	0.988(4)
Zn6	2	1	1	1/4	0.0140(9)	0.664(4)

Table 3 Refined atomic displacement parameters for the basic structure of YZn_{5+x}.

Site	U_{II}	U_{22}	U_{33}	U_{12}	U_{I3}	U_{23}
Y	0.0123(4)	0.0104(3)	0.0102(3)	0.00617(19)	0	0.0067(7)
Zn1	0.0118(4)	0.0130(3)	0.0099(4)	0.0059(2)	0	0.0002(12)
Zn2	0.0115(3)	0.0115(3)	0.0134(5)	0.00577(16)	0	0
Zn3	0.0115(4)	0.0122(9)	0.0108(4)	0.0040(9)	-0.0017(3)	-0.0004(11)
Zn4	0.0162(6)	0.0147(4)	0.0140(3)	0.0102(7)	0.0002(8)	0.0006(2)
Zn5	0.0149(6)	0.0149(6)	0.029(3)	0.0074(3)	0	0
Zn6	0.0144(7)	0.0144(7)	0.013(2)	0.0072(4)	0	0

Powder X-ray Diffraction Analysis. Phase analysis of the sample was performed using powder X-ray diffraction measurements. The sample was ground to a fine powder and placed on a zero-background plate. Diffraction intensities were measured on a Bruker D8 Advance Powder Diffractometer fitted with a LYNXEYE detector, using Cu K α radiation (λ = 1.5418 Å) at ambient temperature. An exposure time of 1.0 second per 0.010° increment was used over the 2 θ range 30-80°.

Wavelength Dispersive X-ray Spectroscopy. To determine the elemental composition of YZn_{5+x} , wavelength dispersive X-ray spectroscopy (WDS) was performed on a sample whose powder X-ray diffraction pattern showed this to be the major phase. To prepare the sample for WDS measurements, a

small amount of material was suspended in a conductive epoxy at one end of a short segment of an aluminum tube. Once the epoxy had hardened, the sample was ground down to produce a flat surface and then polished to reduce the number of surface scratches using a diamond lapping film (Precision Surface International Inc., $0.5 \mu m$). Finally, the sample was carbon-coated. WDS measurements guided by back-scattered electron images were taken with a Cameca SX-Five FE-EMPA Microprobe, using Y_2O_3 , elemental Zn, elemental Si, and ZnO as standards for the Y L α , Zn K α , Si K α , and O K α transitions, respectively.

3. Results and Discussion

3.1. Synthesis of incommensurately modulated YZn_{5+x} crystals

In our earlier investigation of the disordered YZn_{5+x} ($x\approx0.2$) structure, we uncovered channels of disordered Zn atoms running along the **c**-axis, making this compound a member of the EuMg_{5+x} type (Fredrickson *et al.*, 2022). We also noted, however, that a mechanism exists for the communication between the occupants of neighboring channels, opening a path to a potential ordered superstructure. Based on these interactions, we proposed a model for a $\sqrt{3}\times\sqrt{3}\times3$ superstructure. In our attempt to synthetically realize this superstructure, we carried out a modified version of our synthetic procedure. As before we pressed mixtures of the elements into pellets, brought them to a melt at 1100 °C for 24 hours and held them at 500 °C for 1 week for crystal growth. This time, however, rather than quenching the samples in ice water, we introduced a controlled cooling step (10 °C/hour) to encourage superstructure formation. The reaction resulted in relatively large well-defined crystals, particularly in comparison to the quenched products from our previous syntheses containing the disordered YZn_{5+x} crystals. The crystals are metallic grey in color, with smooth surfaces, and are easy to grind into powders. In addition, the crystals exhibit high stability in air with no visible decomposition.

The powder X-ray diffraction data collected for a sample from which we picked the single crystal of YZn_{5+x} (*x*=0.217) is presented in Figure 2. All the major peaks are indexed to the YZn_{5+x} structure by reference to the single crystal data described below. Some minor peaks are assigned to a secondary phase, Y₂Zn₁₇, as well as others that appear to arise from an unknown, third phase. These results are consistent with metallographic analysis of a polished sample with back-scattered electron (BSE) imaging and wavelength dispersive spectroscopy (WDS). BSE revealed two prominent phases in the sample: one appearing lighter, the other darker. The composition for the first of these was determined to be YZn_{5.26(3)} from an average over 43 points, which corresponds closely with that expected for YZn_{5+x}. The second phase has the composition Y₂Zn_{16.81(8)} (average over 30 points); this is assigned as the compound Y₂Zn₁₇. Needle-like domains of a third, minor phase with approximate composition YZn_{2.2}Si_{0.6} were also occasionally observed, which apparently results from a reaction with SiO₂ from the fused silica ampoule. Altogether, though, the powder X-ray diffraction pattern and WDS analysis indicates the YZn_{5+x} is a major phase in the reaction product.

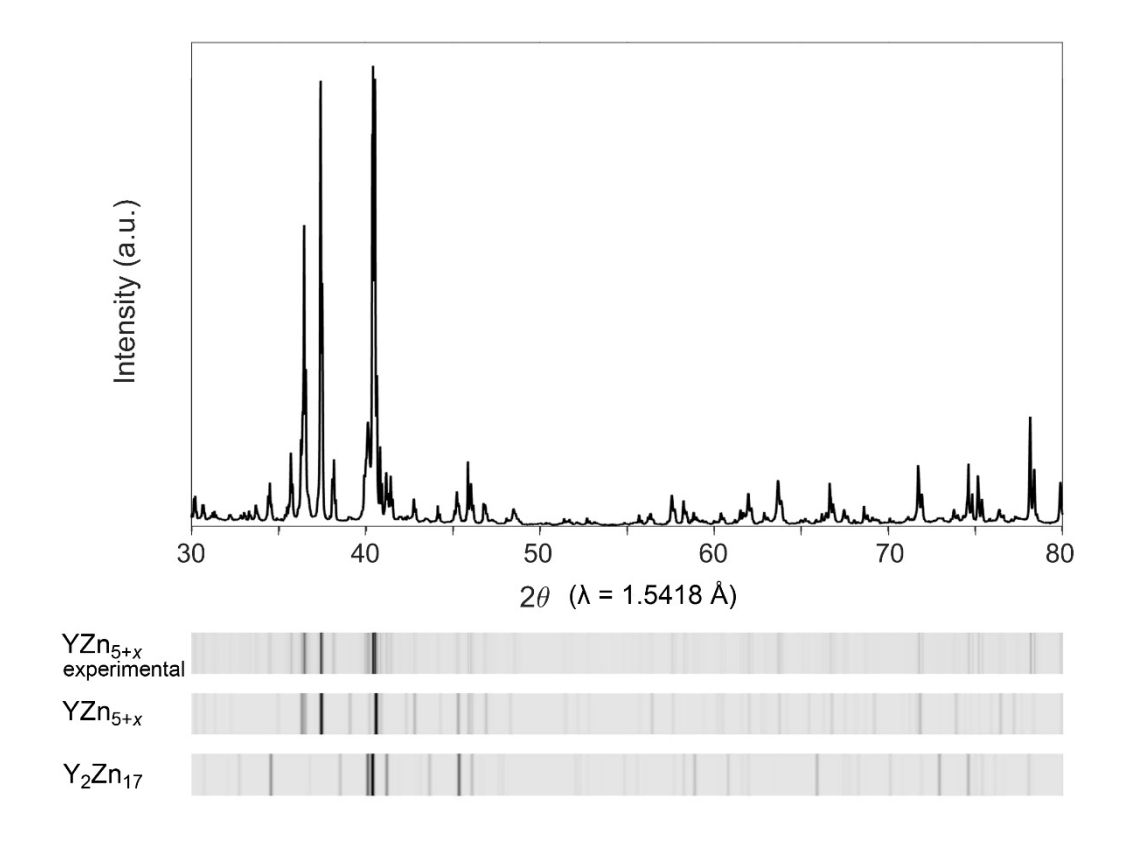


Figure 2 Powder X-ray diffraction pattern of the modulated form of YZn_{5+x} (radiation: Cu Kα, $\lambda = 1.5418$ Å). Top: The experimental data plotted in a 2θ vs. intensity form. Bottom: Filmstrip style representation of the experimental data along with the simulated patterns for YZn_{5+x} and Y₂Zn₁₇.

3.2. Analysis of Diffraction Pattern and Symmetry

Crystals picked from these reaction products exhibit more complex diffraction patterns (Figure 3a) than those obtained from quenching the samples from the annealing temperature. The strongest reflections can be indexed to a hexagonal cell, corresponding to the EuMg_{5+x} type basic structure, with dimensions a = 8.8811(1) Å and c = 9.2057(1) Å. Additional weaker reflections are present in the spaces between these main peaks, as is evident in the reconstruction of the (hhl) layer of reciprocal space (Figure 3). These new reflections correspond approximately to a $\sqrt{3} \times \sqrt{3} \times 3$ supercell, but the distribution of their intensities is highly organized. They trace out rectangles, with the closest reciprocal lattice points of the basic cell being the systematically absent l = odd positions (e.g. hhl = 113, 223 etc.). A careful investigation for the positions of the superstructure reflections reveals that they are all separated from an absent main reflection by one of two vectors: $\mathbf{q} = \frac{1}{2}\mathbf{a}^* + \frac{1}{2}\mathbf{b}^* + 0.3041\mathbf{c}^*$ or $\mathbf{q}^* = -\frac{1}{2}\mathbf{a}^* - \frac{1}{2}\mathbf{b}^* + 0.3041\mathbf{c}^*$, as shown in Figures 3b and 3c, each of which creates a pattern with trigonal symmetry. No other reflections associated with a supercell are evident, suggesting that a superspace approach that considers the additional peaks to arise from modulations will be the most efficient route to solving the structure. In particular, a (3+1)D model (Smaalen, 2007) can be created when we assign

q and **q'** as belonging to separate twin domains, which are related by a 6-fold rotation around \mathbf{c}^* , inline with the hexagonal symmetry of the EuMg_{5+x} type basic structure. While there are several multiples of 60° that could be used to generate these twin domains, the 3-fold symmetry of the individuals will lead to only two symmetry-distinct crystal orientations.

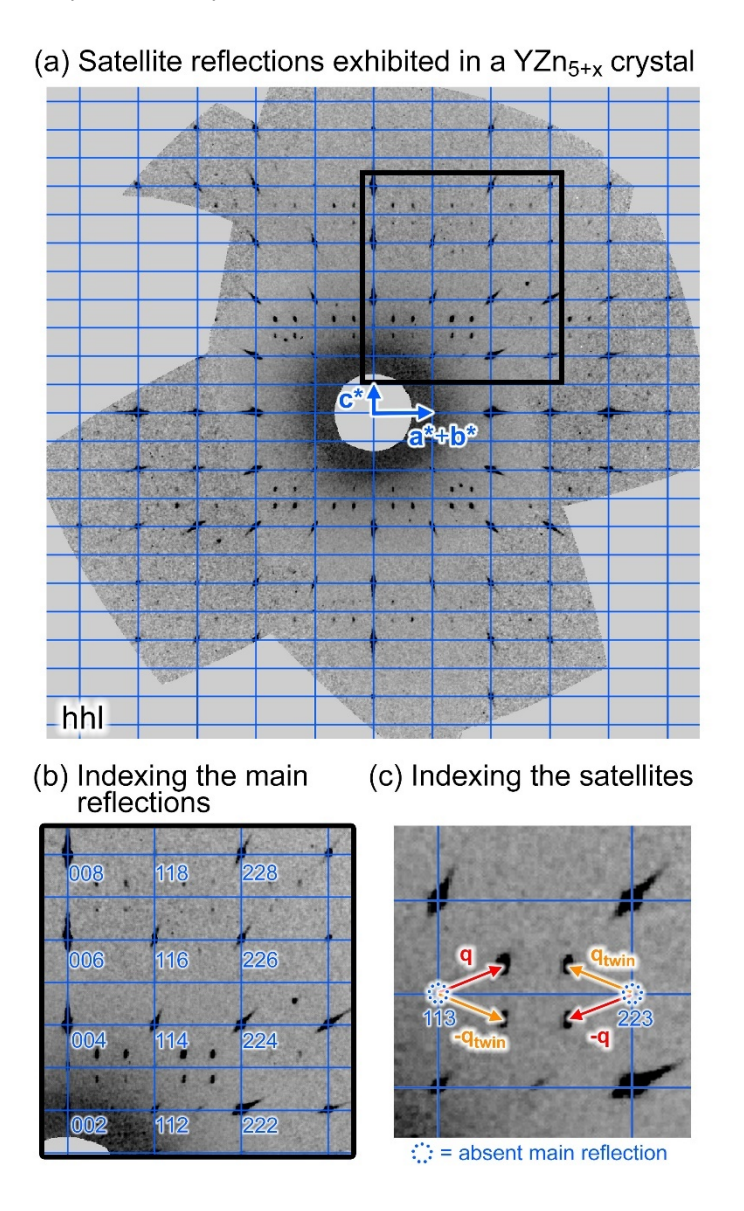


Figure 3 Diffraction pattern of a YZn_{5+x} (x=0.217) crystal. (a) The satellite reflections exhibited along with the strong main reflections in the hhl plane. (b) Enlarged area, with the indices of the main reflections. (c) Indexation of the satellite reflections with the modulation wave vector ($\mathbf{q} = \frac{1}{3}\mathbf{a}^* + \frac{1}{3}\mathbf{b}^* + 0.3041\mathbf{c}^*$) (red) and the corresponding vector for a twin domain (orange). Dotted blue circles denote absent main reflections.

In this approach, the experimental diffraction pattern is interpreted as the projection on 3D of a (3+1)D array of reflections, with the satellites having a component along the 4th dimension. The corresponding real space construction is a periodic structure in (3+1)D from which the physical

incommensurately modulated structure is obtained by taking 3D cross-sections. The direction perpendicular to the physical cross-section is given by the \mathbf{a}_{s4} -axis, which represents the superspace lattice vector for the modulation function, while the \mathbf{a}_{s1} -, \mathbf{a}_{s2} -, and \mathbf{a}_{s3} -axes are counterparts to the physical \mathbf{a} -, \mathbf{b} -, and \mathbf{c} -axes. They are, however, tilted out of physical space in accordance with how much the phase of the modulation function changes for translations along the \mathbf{a} , \mathbf{b} , and \mathbf{c} repeat vectors.

A first step in building such a model is the assignment of the structure's (3+1)D superspace group. The **q**-vector $\mathbf{q} = \frac{1}{3}\mathbf{a}^* + \frac{1}{3}\mathbf{b}^* + 0.3041\mathbf{c}^*$ gives rise to a trigonal arrangement of satellite reflections, which is incompatible with the hexagonal space group $P6_3/mmc$ of the EuMg_{5+x} type. In terms of potential trigonal subgroups of $P6_3/mmc$, we observe that the systematic absence condition associated with the c glide in $P6_3/mmc$, hhl: l = 2n, still applies to the main reflections (Figure 3), suggesting that the superspace group of the modulated structure is based on the $P6_3/mmc$ subgroup $P\overline{3}1c$. When we consider the full set of reflections, it is notable that the satellites only appear in the layer when l is odd, pointing to the condition hhlm: l+m=2n. In terms of the symmetry operations of the (3+1)D superspace group, this corresponds to the c glide operation in 3D space being accompanied by a shift in the phase of the modulation (x_4) by $\frac{1}{2}$. Altogether, these considerations indicate that the highest possible superspace group is $P\overline{3}1c(\frac{1}{3}\frac{1}{3}a_3)00s$.

3.3. Structure solution and refinement

In the structure solution process, the charge flipping algorithm using the program *Superflip* converged on a (3+1)D electron density corresponding to the experimental diffraction intensities. The automated symmetry search and peak analysis of this electron density map agreed with the assignment of the superspace group as $P\overline{3}1c(\frac{1}{3}\frac{1}{3}\sigma_3)00s$, and yielded the basic framework of the EuMg_{5+x} type basic structure. In addition, two atomic domains associated with the disordered channels in the EuMg_{5+x} type were identified, which we label Zn5 and Zn6.

The electron density features for the Zn5 and Zn6 sites show strong modulations with both occupational and positional components (Figure 4a and 4b). For the Zn5 site, the electron density contours in x_3 - x_4 section trace out nearly linear domains centered at x_4 = 0.5 that are slanted to give a negative slope, and end on discontinuities near x_4 = 0.0 and 1.0. Similar features are found for the Zn6 site, except that then domain is centered at x_4 = 0.75, and their length along x_4 is shorter, with the width Δx_4 being about $\frac{2}{3}$. To model the discontinuous nature of these domains, we used crenel functions (Petříček *et al.*, 2016) centered at x_4 = 0.5 and x_4 = 0.75 for Zn5 and Zn6 respectively, with the corresponding Δx_4 values initially being set to 1.0 and $\frac{2}{3}$, where the latter is a close rational approximant to $\frac{1}{2}$ + $\frac{1}{2}$ σ_3 (the Δx_4 width for Zn6 needed to match the ends of the Zn5 and Zn6 domains in the physical cross-sections; see the Supporting Information). This is convenient as σ_3 varies from crystal to crystal (in the range of 0.304 to \sim 0.331). In addition, first order positional modulations (based on Legendre

polynomials tailored to the Δx_4 width of the domain) were applied to allow the atomic domains to slant in the x_3 - x_4 plane.

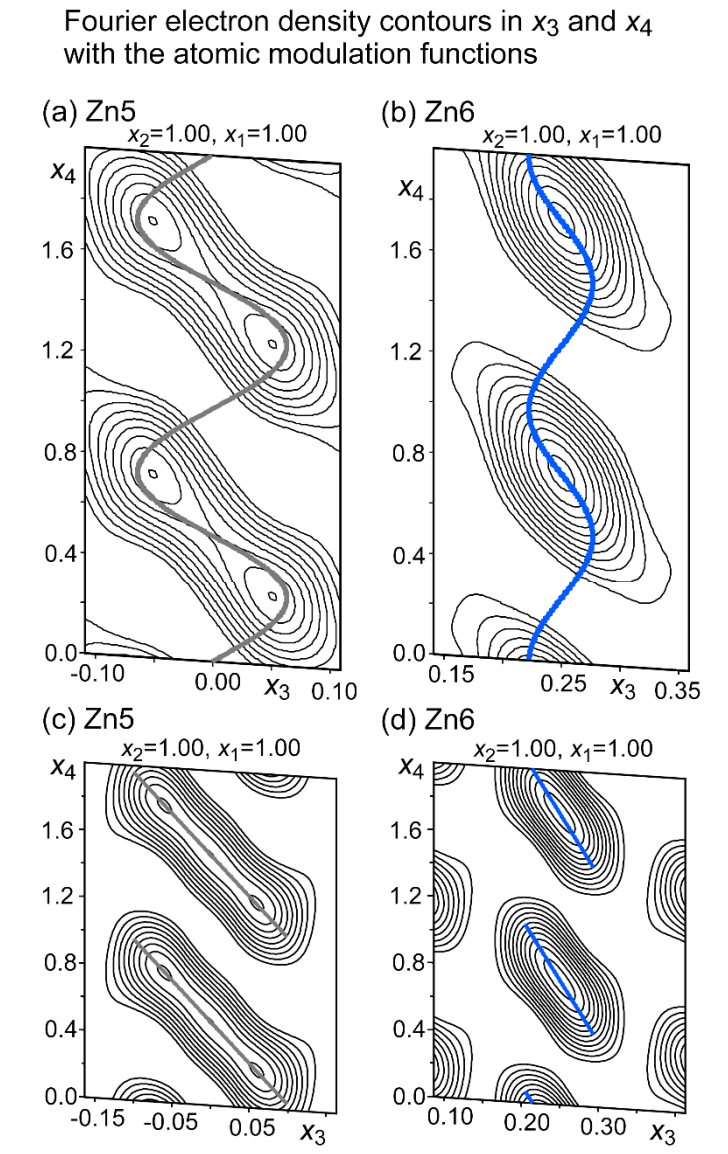


Figure 4 Contour maps of the Fourier electron density for (x_3, x_4) cross-sections through the Zn5 and Zn6 atomic domains. Top: the contours generated from the structure solution for the (a) Zn5 and (b) Zn6 sites show positionally modulated and discontinuous atomic domains. Bottom: the contours of refined atomic modulation functions with crenel functions for the (c) Zn5 and (d) Zn6 sites. The model positions for Zn5 and Zn6 are shown in gray and blue, respectively.

After setting these modulation functions for the Zn5 and Zn6 sites, in addition to first order harmonic positional waves on the remaining atoms, the refinement led quickly to a drop in the R-factors for the satellite reflections. However, additional corrections were needed for a successful refinement. First, a twin component was included whose reciprocal lattice is rotated around the **c**-axis by 60°, reflecting the hexagonal symmetry of the parent structure. Curiously, though, the twin-fraction

invariably refined to approximately 0.75, regardless of which individual is integrated. As the diffraction patterns for the individuals overlap only on the main reflections, this suggested that the main reflections are systematically too strong relative to the satellites. Interpreting this as arising from disordered domains in the crystal, we used separate scale factors for the main and satellite reflections. Upon doing so, the twin fractions converged to 0.50, within two times the standard uncertainty, indicating that the crystal has balanced twinning.

In the final model, all the atoms are refined anisotropically, and first order modulations were applied to the harmonic atomic displacement parameters for all atoms but Zn6, with its relatively short and discontinuous domains. In addition, the Δx_4 widths for Zn5 and Zn6 were refined with the restraint that the edges of their atomic domains are aligned for clean transitions in the physical cross-sections, as in $\Delta x_4[\text{Zn6}] = \frac{1}{2} + \frac{1}{2}\sigma_3 + (1 - \Delta x_4[\text{Zn5}])$, yielding values of 0.988(3) and 0.664(4), respectively. The refined model positions for the Zn5 and Zn6 sites are compared to the Fourier electron density contours in Figures 4c, 4d. In both cases, the model consists of slanted lines that align closely with the density features.

3.4. Structural interpretation of the modulated model

The nature of the modulation pattern is simple to interpret in terms of the disordered channels of the EuMg_{5+x}-type form of YZn_{5+x} described previously (Figure 1a) and the (3+1)D Fourier electron densities for the corresponding atomic sites in the current structure. The Y and Zn1-Zn4 sites define the host structure of the EuMg_{5+x} type, and their electron density features are well-described by harmonic functions with relatively small amplitudes (see Figure S2 in the Supporting Information). By contrast, the Zn5 and Zn6 sites corresponding to the occupants of the channels have discontinuous atomic domains, indicating much stronger modulations. The Zn5/Zn6 sites can thus be seen as the

major drivers of the modulation, with the positional displacements on the remaining atoms serving as adjustments to accommodate the resulting changes in their local environments.

The structural consequences of the Zn5/Zn6 site modulations become clearer when looking at a larger cross-section for the (x_3, x_4) plane containing them (Figure 5). Zn5 and Zn6 domains alternate as we move from left to right on the physical axis, corresponding to the centers of the flattened octahedra and tricapped trigonal prisms whose alternation builds up the channel walls. While the Zn5 and Zn6 sites are made distinct by their association with these two different polyhedra, their domains show a high degree of correlation: their electron density features are both slanted from upper left to lower right, and following one domain down this slope brings one to right to the tip of the next atomic domain, on the other side of a small gap.

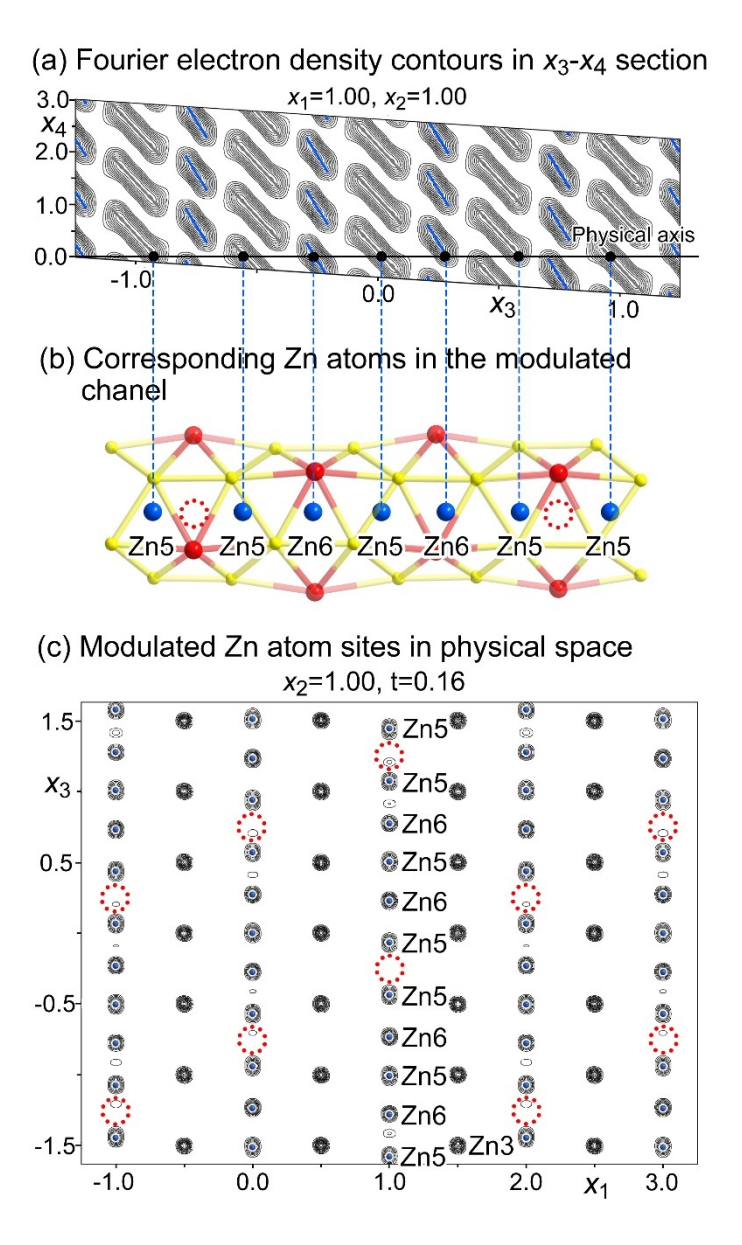


Figure 5 Connection between the (3+1)D Fourier electron density and structural features in physical space. (a) Fourier electron density contours corresponding to the Zn5 and Zn6 sites in an x_3 - x_4 section. (b) The corresponding modulated channel containing Zn5 and Zn6 atoms in physical space. (c) Modulated Zn5 and Zn6 sites in physical space laid over the Fourier electron density map of the xz plane of a 3D density constructed from the (3+1)D model (t-section). Such sections can appear somewhat messy due to the density features being broader than the model's atomic domains. The x_4 offset of the cross section off of the origin in (3+1)D space has been adjusted $(t_0 = 0.16)$ to reveal well separated density peaks along the channel. Vacant Zn6 positions are noted with red dotted circles.

In fact, if one were to shrink these gaps, the Zn5 and Zn6 domains would coalesce into diagonal stripes that run with a slant relative to the \mathbf{a}_{s4} -axis. Such a continuous slanted domain would encode a series of equally spaced Zn atoms whose spacing in physical space is mismatched with respect to the remainder of the structure (and determined by the angle of the slant). The high degree to which this

pattern approximates a series of parallel diagonally oriented lines reveals that the Zn atoms in the channel have moved towards an equal spacing that is independent of the host lattice, as in a composite structure (Yamamoto, 1993, Rohrer *et al.*, 2000, Sun *et al.*, 2007). Indeed, the structure can be formally expressed as a composite structure in which the Zn6/Zn5 atoms occupying the channels are described as having their own lattice vector, \mathbf{c}_{guest} , which is incommensurate to that of the host structure, \mathbf{c}_{host} , with $\mathbf{c}_{guest} = \mathbf{c}_{host}/(3+\sigma_3)$. To perform refinements within this composite formalism, one first transforms the cell to a $\sqrt{3} \times \sqrt{3} \times 1$ supercell (to obtain an axial \mathbf{q} -vector) and then assigns the reciprocal basis vectors of the guest composite part (the channel occupants) as $\mathbf{c}_{guest}^* = 3\mathbf{c}_{host}^* + \mathbf{q}_{host}$ and $\mathbf{q}_{guest} = 2\mathbf{c}_{host}^*$. This corresponds to the following transformation matrix connecting the *hklm* indices of reflection in terms of the host and guest composite parts:

$$W = \begin{pmatrix} 1 & 0 & 0 & 0 \\ 0 & 1 & 0 & 0 \\ 0 & 0 & 3 & 2 \\ 0 & 0 & 1 & 0 \end{pmatrix}$$

When implemented, this provides the channel occupants with their own axis in the (3+1)D model. However, two crenel functions are still needed, representing different scenarios for the tricapped trigonal prismatic and flattened octahedral holes in the channels, and the overall R-factors are quite similar to those obtained above.

While a composite model would normally suggest that all points along the host cell's channels can be populated by guest atoms, the gaps between the Zn5 and Zn6 domains suggest that certain points are not suitable. In fact, the gaps correspond approximately in physical space to the centers of flattened Zn₃Y₃ octahedra that lie on opposite sides of the Zn6 sites. An explanation for these gaps can be discerned in the somewhat steeper slope of the Zn6 atomic domains than for the Zn5 atoms. The higher verticality here corresponds to a tighter localization around the average Zn6 position, indicating a preference for the center of the tricapped trigonal prism, where the Y-Zn contacts are shorter.

The features we have discussed so far explain the component of the modulation along the **c**-axis of the EuMg_{5+x} type. The full **q**-vector, $\mathbf{q} = \frac{1}{3}\mathbf{a}^* + \frac{1}{3}\mathbf{b}^* + 0.3041\mathbf{c}^*$, also contains components along the perpendicular directions \mathbf{a}^* and \mathbf{b}^* , indicating that the occupation patterns of neighboring channels differ from each other. In the (3+1)D model, the channels are translationally related by steps of $\Delta x_1 = \pm 1$ and $\Delta x_2 = \pm 1$. In this construction, the non-zero components of σ_1 and σ_2 are reflected in the tilting of the \mathbf{a}_{s1} - and \mathbf{a}_{s2} - axes off the physical \mathbf{a} - and \mathbf{b} -axes, such that points along these axes are given by $(x_1, 0, 0, +\sigma_1 x_1 + t_0)$ and $(0, x_2, 0, +\sigma_2 x_2 + t_0)$, respectively, where t_0 is the intercept with the \mathbf{a}_{s4} axis chosen when making the 3D physical cross-section (and is arbitrary in the case of an incommensurate structure). Since σ_1 and σ_2 are both equal to $\frac{1}{3}$ (as required by the superspace group $P\overline{3}1c(\frac{1}{3}\frac{1}{3}\sigma_3)00s)$, moving from one channel to one of its neighbors along \mathbf{a}_{basic} or \mathbf{b}_{basic} , results in a shift of the modulation phase by $\frac{1}{3}$. These shifts are evident in the electron density maps for the 3D cross section (t-maps,

Figure 5c), where the Zn6 vacancies in neighboring channels are offset from each other by steps of ½ of the spacing between the vacancies along the channel.

This picture can be compared to the $\sqrt{3}\times\sqrt{3}\times3$ superstructure predicted previously from tracing paths of chemical pressure between channels through the TCP units. In this model, every third Zn6 site is vacant within each channel, creating a 3-fold superstructure along c. The occupation patterns of neighboring channels are connected through rhombohedral centering, with the primitive cell vectors being $\mathbf{a}_{prim} = \mathbf{a}_{basic} + \mathbf{c}_{basic}$, $\mathbf{b}_{prim} = \mathbf{b}_{basic} + \mathbf{c}_{basic}$, and $\mathbf{c}_{prim} = -\mathbf{a}_{basic} - \mathbf{b}_{basic} + \mathbf{c}_{basic}$. Transforming this arrangement to the hexagonal setting gives rise to the $\sqrt{3}\times\sqrt{3}\times3$ supercell. In Figure 6, we plot the 3D structure of the incommensurately modulated form of YZn_{5+x} generated from our (3+1)D model. First in Figure 6a, we show a view down \mathbf{c} , color-coding the different channels according to the relative heights of the channel occupation patterns. In this case, the \mathbf{a} and \mathbf{b} vectors of the $\sqrt{3}\times\sqrt{3}\times3$ supercell represent true crystallographic translations, labelled \mathbf{a}_{mod} and \mathbf{b}_{mod} , due to the commensurability of the modulation along these directions. This corresponds to the predicted pattern in the ab-plane, as can be seen by comparison with Figure 1b.

Next, in Figure 6b, we examine the occupation patterns of neighboring channels in more detail. In each channel, every third Zn6 atom is missing in this portion of the structure (red dotted circles), but as these positions are not translationally equivalent points in the basic structure (the EuMg_{5+x}-type unit cell has two Zn6 sites per cell along c) the overall pattern repeats every six Zn6 positions. The neighboring channels are shifted out of step by one Zn6 site, with the Zn6 coordination environments in the same orientation becoming shifted by $\frac{1}{3}$ of the approximate supercell vector along c. If the structure were to be commensurate, this would correspond in all respects to the predicted model.

The close approximation of σ_3 to $\frac{1}{3}$ raises the question of whether a commensurate model may be warranted. To answer this question, we attempted refinements in which σ_3 was set to $\frac{1}{3}$ and the structure was treated as commensurate in terms of the structure factor calculations. Regardless of what t_0 value was chosen, however, the R-factors for the model were unreasonably high (overall R[I > 3σ] >10.0 vs. 2.7 for the incommensurately modulated model). The incommensurability of the phase is further supported by the observation that the σ_3 value obtained from the diffraction patterns of different crystals can vary from 0.304 to 0.331 (in fact, some slight splitting of the satellites into closely spaced pairs of σ_3 values can be detected in the reciprocal lattice reconstructions). As such, the spacing of Zn atoms along the structure's channels appears not to be locked into registry with the c parameter of the host structure.

How, then, does the incommensurately modulated structure differ from the idealized three-fold superstructure along c? As we mentioned above, the σ_3 value in the (3+1)D model controls the average spacing of the Zn atoms occupying the channels, \mathbf{c}_{guest} , relative to the c parameter of the host sublattice's average structure, \mathbf{c}_{host} , as in $\mathbf{c}_{guest} = \mathbf{c}_{host}/(3+\sigma_3)$. For $\sigma_3 = 1/3$, this gives rise to a commensurate

arrangement with 3 \mathbf{c}_{host} = 10 \mathbf{c}_{guest} , i.e. 10 Zn5/Zn6 atoms in a 3-fold supercell of the disordered EuMg_{5+x} type structure, matching that of the originally predicted superstructure with composition YZn_{5.225}. For lower σ_3 values, the average spacing of the channel atoms increases, leading to a lower overall Zn content of YZn_{5+(1+\sigma_3)/6}, e.g. YZn_{5.217} for σ_3 = 0.3041, with each atom in the channel locking into a nearby Zn5 or Zn6 atomic domain.

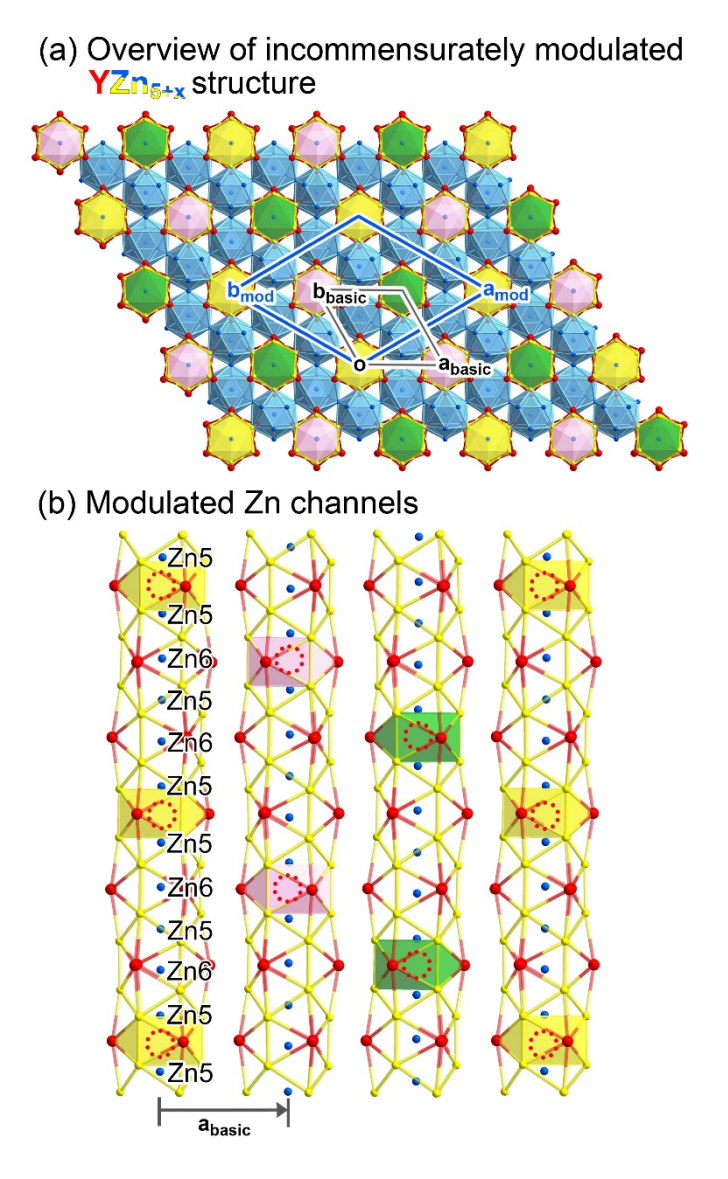


Figure 6 Incommensurately modulated YZn_{5+x} (x=0.217) structure. (a) Overview of the structure viewed down [001]. (b) The modulated Zn channels with the one-third shift pattern (yellow, pink, and green). Vacant Zn6 positions are noted with red dotted circles.

4. Conclusions

In our earlier analysis of EuMg_{5+x}-type YZn_{5+x}, we identified paths of chemical pressures between its disordered channels that point to a potential ordered superstructure. In this article, we have confirmed this picture experimentally, demonstrating that, through a change to the synthetic procedure,

YZn_{5+x} crystals with satellite reflections from channel order can be obtained. In this pattern, approximately every third Zn6 position within the channel is vacant, with the remaining occupants exhibiting displacements that serve to smooth out the spacing between them. Between neighboring channels, shifts in the pattern arise to stagger the positions of the vacancies, which we had predicted would minimize the accumulation of packing tensions along paths of inter-channel contacts. Rather than the expected $\sqrt{3} \times \sqrt{3} \times 3$ supercell of the EuMg_{5+x} type, however, the pattern is incommensurate along the **c**-axis, as revealed by variability in the σ_3 parameter of the **q**-vector and the satellite intensity distributions.

These results contribute to a growing theme in the structural chemistry of intermetallics: the communication of information between different regions of a crystal structure through paths of chemical pressures (CPs). For example, the remarkably large hysteresis in the cubic to tetragonal phase transition of PtGa₂ was interpreted in terms of the tight coordination of atomic motion imposed by its CP scheme (Mitchell Warden *et al.*, 2018). Similarly, the unusual, slanted domains of the trimermonomer patterns in the incommensurately modulated IrSi structure (Mitchell Warden & Fredrickson, 2019), as well as the form of the low-temperature superstructure and high-temperature incommensurability in PdBi (Folkers *et al.*, 2020), were traced to the domino-like propagation of atomic displacements that create emergent, long-range patterns. In these cases, the explanations for the detailed choreographies of atomic motions benefited from knowing the structural solution beforehand. With the example of YZn_{5+x}, we see more clearly how this approach can be used in a predictive fashion: Beginning with CP schemes for a handful of ordered models, the Zn site occupancies in the average structure, and hints from the literature about the size of the expected supercell, an ordering pattern could be proposed, which could then be successfully realized synthetically.

An open challenge highlighted by this work is the question of whether such ordering patterns will adopt commensurate or incommensurate arrangements. Could the incommensurability in YZn_{5+x} have been predicted ahead of time? In this case, the CP features offer clear indications of how the occupation patterns of neighboring channels are coupled, but give less guidance on the preferred sequence along the channels. Instead, our original model used experimental Zn occupancies in the average structure, and assumed the vacancies would be distributed at regular intervals. There is room within that scheme for these intervals to be mismatched from the c period of the host lattice, but there was not an obvious reason for this being advantageous. One potential hint to a driving force for more Zn6 occupancy is seen in the large positive CPs taken on by Zn5 sites neighboring a Zn6 vacancy, as they move in to smooth out the Zn-Zn distances along the channel. Incommensurability would allow the structure to tune the Zn6 vacancy concentration to balance the benefits of a sparser occupation of the channels with the energetic costs to the Zn5 sites neighboring the vacancies. It will be interesting to see whether

theoretical models, based on CP analysis or other tools, can be developed to detect such situations where incommensurability provides an opportunity to balance competing factors.

Acknowledgements We gratefully acknowledge Dr. William Nachlas and Bil Schneider (UW-Madison Geosciences) for assistance with the WDX measurements, as well as Prof. Sven Lidin for discussions regarding the formal modeling of YZn_{5+x} as a composite structure.

References

Becker, H. & Leineweber, A. (2018). Intermetallics 93, 251-262.

Berns, V. M. & Fredrickson, D. C. (2013). Inorg. Chem. 52, 12875-12877.

Berns, V. M. & Fredrickson, D. C. (2014). Inorg. Chem. 53, 10762-10771.

Bohdana, B., Mykola, M., Mariya, D., Dorota, K. & Roman, G. (2020). *Ukrainian Chemistry Journal* **86**, 3-12.

Bruzzone, G., Fornasini, M. L. & Merlo, F. (1970). J. Less Common Met. 22, 253-264.

Erassme, J. & Lueken, H. (1987). Acta Crystallogr. B: Struct. Sci. 43, 244-250.

Etzkorn, J., Ade, M. & Hillebrecht, H. (2007). Inorg. Chem. 46, 7646-7653.

Feuerbacher, M., Thomas, C., Makongo, J. P. A., Hoffmann, S., Carrillo-Cabrera, W., Cardoso, R., Grin, Y., Kreiner, G., Joubert, J. M., Schenk, T., Gastaldi, J., Nguyen-Thi, H., Mangelinck-Noel, N., Billia, B., Donnadieu, P., Czyrska-Filemonowicz, A., Zielinska-Lipiec, A., Dubiel, B., Weber, T., Schaub, P., Krauss, G., Gramlich, V., Christensen, J., Lidin, S., Fredrickson, D., Mihalkovic, M., Sikora, W., Malinowski, J., Bruhne, S., Proffen, T., Assmus, W., de Boissieu, M., Bley, F., Chemin, J. L., Schreuer, J. & Steurer, W. (2007). Z.Kristallogr. 222, 259-288.

Folkers, L. C., Mitchell Warden, H. E., Fredrickson, D. C. & Lidin, S. (2020). *Inorg. Chem.* **59**, 4936-4949.

Fornasini, M. L. (1971). J. Less Common Met. 25, 329-332.

Fredrickson, R. T., Kamp, K. R. & Fredrickson, D. C. (2022). Z. Anorg. Allg. Chem. 648, e202200068.

Frey, F. (1995). Acta Crystallogr. B 51, 592-603.

Gladyshevskii, R. E., Strusievicz, O. R., Cenzual, K. & Parthé, E. (1993). *Acta Crystallogr. B* 49, 474-478.

Hilleke, K. P. & Fredrickson, D. C. (2018). J. Phys. Chem. A 122, 8412-8426.

Janner, A. & Janssen, T. (1980a). Acta Crystallogr. A 36, 399-408.

Janner, A. & Janssen, T. (1980b). Acta Crystallogr. A 36, 408-415.

Keen, D. A. & Goodwin, A. L. (2015). Nature 521, 303-309.

Larsson, A. K., Withers, R. L. & Stenberg, L. (1996). J. Solid State Chem. 127, 222-230.

Lidin, S., Christensen, J., Jansson, K., Fredrickson, D., Withers, R., Noren, L. & Schmid, S. (2009). *Inorg. Chem.* 48, 5497-5503.

Lu, E. & Fredrickson, D. C. (2019). Inorg. Chem. 58, 4063-4066.

Lu, E., Van Buskirk, J. S., Cheng, J. & Fredrickson, D. C. (2021). Crystals 11, 906.

Mitchell Warden, H. E. & Fredrickson, D. C. (2019). J. Am. Chem. Soc. 141, 19424-19435.

Mitchell Warden, H. E., Voyles, P. M. & Fredrickson, D. C. (2018). Inorg. Chem. 57, 13880-13894.

Mühlpfordt, W. (1970). Z. Anorg. Allg. Chem. 374, 174-185.

Mühlpfordt, W. (1997). Z. Anorg. Allg. Chem. 623, 985-989.

Okamoto, N. L., Okumura, J., Higashi, M. & Inui, H. (2017). Acta Mater. 129, 290-299.

Oszlányi, G. & Sütő, A. (2004). Acta Crystallogr. Sect. A: Found. Crystallogr. 60, 134-141.

Oszlányi, G. & Sütő, A. (2005). Acta Crystallogr. Sect. A: Found. Crystallogr. 61, 147-152.

Palatinus, L. (2004). Acta Crystallogr. A 60, 604-610.

Palatinus, L. & Chapuis, G. (2007). J. Appl. Crystallogr. 40, 786-790.

Peterson, G. G. C., Geisler, E. E. & Fredrickson, D. C. (2020). Inorg. Chem. 59, 5018-5029.

Petříček, V., Dušek, M. & Palatinus, L. (2014). Z. Kristallogr. 229, 345-352.

Petříček, V., Eigner, V., Dušek, M. & Čejchan, A. (2016). 231, 301-312.

Rohrer, F. E., Lind, H., Eriksson, L., Larsson, A. K. & Lidin, S. (2000). Z. Kristallogr. 215, 650-660.

Smaalen, S. v. (2007). *Incommensurate crystallography*. Oxford; New York: Oxford University Press.

Sun, J., Lee, S. & Lin, J. (2007). Chem. Asian J. 2, 1204-1229.

Vinokur, A. I., Hilleke, K. P. & Fredrickson, D. C. (2019). Acta Crystallogr. A 75, 297-306.

Yamamoto, A. (1993). Acta Crystallogr. Sect. A: Found. Crystallogr. 49, 831-846.

Supporting information

S1. Derivations of Relationships for the (3+1)D Modeling of YZn_{5+x}

Crenel function Δx_4 parameters for the Zn5 and Zn6 sites. The Δx_4 parameter for an atomic domain described with a crenel function gives the length of the interval along the x_4 (centered at $x_{4,0}$) for which the atom is present. With the slanting of the atomic domains in the (x_3,x_4) planes in Figure 5, the upper left tip of the Zn6 domains closely approaches the lower right tip of the Zn5 domain whose center is displaced by $(-\frac{1}{4},\frac{3}{4})$ from the Zn6 center. On the other side of the Zn6 domain, its lower right tip comes close to the upper left tip of the Zn5 domain whose center is offset from the Zn6 center by $(\frac{1}{4},-\frac{3}{4})$. A continuous coverage for the x_4 axis by each Zn5/Zn6 line can be obtained by lining up the ends of the domains so that their tips occur at the same lines perpendicular to the x_4 axis, parallel to the physical z axis. On the left side of the Zn6 domain, this will occur when $\frac{3}{4}-\frac{\Delta x_4[Zn5]}{2+\sigma_3/4} = \frac{\Delta x_4[Zn6]/2}{2}$, where $\frac{\sigma_3}{4}$ is the shift along x_4 needed to stay on the physical z-axis after moving $\frac{1}{4}$ along x_3 . Similarly, on the right side the match along z is achieved with $-\frac{\Delta x_4[Zn6]}{2+\sigma_3/4} = -\frac{3}{4} + \frac{\Delta x_4[Zn5]}{2}$. Using either equation, we obtain $\frac{\Delta x_4[Zn6]}{2} = \frac{1}{2} + \frac{\sigma_3}{2} + \frac{1}{2} + \frac{\sigma_3}{2}$. In the special case where $\frac{\Delta x_4[Zn5]}{2} = 1$, this yields $\frac{\Delta x_4[Zn6]}{2} = \frac{1}{2} + \frac{\sigma_3}{2}$.

Relationship between the c_{host} and c_{guest} in the composite description of YZn_{5+x}. From Figure 5, note that the slanted lines created by the Zn5 and Zn6 atomic domains have an average slope of $\Delta x_4/\Delta x_3 = -3/1$. If we label these slanted lines with the index j, the coordinates on the points of line j will be given by $(x_{3,j},0) + \varepsilon(-1,3)$, where $x_{3,j}$ is the intercept of the line with the x_3 axis, and ε is a free variable. The z coordinate in physical space of the atom arising from line j can be derived by setting $z = (x_3, x_4) = (x_3, \sigma_3 x_3)$ equal to $(x_{3,j},0) + \varepsilon(-1,3)$. From this we find $x_3 = x_{3,j} - \varepsilon$ and $\sigma_3 x_3 = 3\varepsilon$. Solving for x_3 in terms of $x_{3,j}$, we arrive at $x_3 = x_{3,j}/(1+\sigma_3/3)$ as the coordinate where the line intersects the physical z axis. As the slanted lines divide each repeat vector along x_3 into three intervals, the average space between two neighboring Zn atoms along z in the channel is one third of $1/(1+\sigma_3/3)$, i.e. $1/(3+\sigma_3)$. Since these numbers represent fractions of the c lattice vector of the host average structure, we have $c_{guest} = c_{host}/(3+\sigma_3)$.

The composition of YZn_{5+x} in terms of σ_3 . One average cell of the host structure has the contents Y_6Zn_{28} and contains one channel. The channel contains Zn atoms spaced at intervals of $\mathbf{c}_{\mathbf{guest}}$, giving on average $c_{host}/c_{guest} = 3+\sigma_3$ atoms per host cell. Altogether, the composition of the phase is then $Y_6Zn_{28+3+\sigma_3} = Y_6Zn_{31+\sigma_3}$ or $YZn_{5+(1+\sigma_3)/6}$.

S2. Crystallographic Information Tables for the (3+1)D model of YZn_{5+x}

Detailed tables are given describing the atomic coordinates, atomic displacement parameters, and modulation functions refined for the (3+1)D model of YZn_{5+x} .

Table S1 Modulation parameters for YZn_{5+x} .

Crenel Functions	Atomic sites	Δ	x_{40}
	Zn5	0.988(4)	0.5
	Zn6	0.664(4)	0.75

Legendre Polynomial (xyz)	Atomic sites	N	$S_{x,n}(odd)$	$S_{y,n}(odd)$	$S_{z,n}(odd)$	$S_{x,n}(even)$	$S_{y,n}(even)$	$S_{z,n}(even)$
	Zn5	1	0	0	-0.0996(9)	0	0	0
	Zn6	1	0	0	-0.0447(8)	0	0	0

Harmonic (xyz)	Atomic sites	N	$U_{x,n}(\sin)$	U _{y,n} (sin)	$U_{z,n}(\sin)$	$U_{x,n}(\cos)$	$U_{y,n}(\cos)$	$U_{z,n}(\cos)$
	Y	1	0.00386(10)	0.0044(2)	-0.00165(19)	0.0102(3)	0.00417(17)	0.00062(7)
	Zn1	1	-0.0021(3)	0.00028(17)	0.00036(10)	-0.00096(12)	-0.0035(5)	-0.0008(2)
	Zn2	1	-0.0014(2)	0.0035(3)	0	-0.0048(3)	-0.0036(3)	0
	Zn3	1	-0.0039(3)	-0.0020(3)	0.0014(2)	0	0	0
	Zn4	1	-0.0035(2)	-0.0043(2)	0.00202(19)	-0.0039(2)	-0.0094(2)	-0.00357(19)

Harmonic (ADP)	Atom sites	N	U _{11,n} (sin)	U _{22,n} (sin)	U _{33,n} (sin)	$U_{12,n}(\sin)$	$U_{13,n}(\sin)$	$U_{23,n}(\sin)$
	Y	1	0.0014(4)	-0.0005(7)	0.0002(4)	-0.0002(7)	-0.0004(8)	-0.0007(5)
	Zn1	1	-0.0002(12)	-0.0011(9)	0.0003(12)	-0.0010(7)	0.0001(4)	0.0004(8)
	Zn2	1	-0.0007(9)	0.0013(9)	0	0.0006(13)	0.0004(11)	0.0009(9)
	Zn3	1	0	0	0	0	0	0
	Zn4	1	0.0001(10)	0.0035(10)	-0.0039(10)	0.0015(8)	0.0001(8)	0.0014(7)

Harmonic (ADP)	Atom sites	N	$U_{11,n}(\cos)$	$U_{22,n}(\cos)$	$U_{33,n}(\cos)$	$U_{12,n}(\cos)$	$U_{13,n}(\cos)$	$U_{23,n}(\cos)$
	Y	1	0.0036(9)	0.001(3)	0.0006(10)	0.0022(6)	0.0001(3)	-0.0013(18)
	Zn1	1	-0.0001(5)	0.002(2)	0.0002(5)	0.002(2)	-0.0002(9)	0.0000(7)
	Zn2	1	0.0011(12)	0.0001(11)	0	0.0011(7)	-0.0008(12)	0.0001(14)
	Zn3	1	0.0025(13)	0.0004(13)	-0.0042(12)	0.0016(11)	0.0000(12)	-0.0008(11)
	Zn4	1	-0.0019(10)	-0.0017(9)	0.0005(9)	-0.0012(8)	-0.0003(8)	-0.0012(7)

Legendre Polynomial	Atomic							
(ADP)	sites	N	$S_{11,n}(odd)$	$S_{22,n}(odd)$	$S_{33,n}(odd)$	$S_{12,n}(odd)$	$S_{13,n}(odd)$	$S_{23,n}(odd)$
	Zn5	1	0	0	0	0	0	0

Legendre Polynomial	Atomic							
(ADP)	sites	N	$S_{11,n}(even)$	$S_{22,n}(even)$	$S_{33,n}(even)$	$S_{12,n}(even)$	$S_{13,n}(even)$	$S_{23,n}(even)$
	Zn5	1	-0.008(3)	-0.008(3)	-0.016(6)	-0.0038(13)	0	0

S3. Wavelength Dispersive X-ray Spectroscopy (WDS) Results

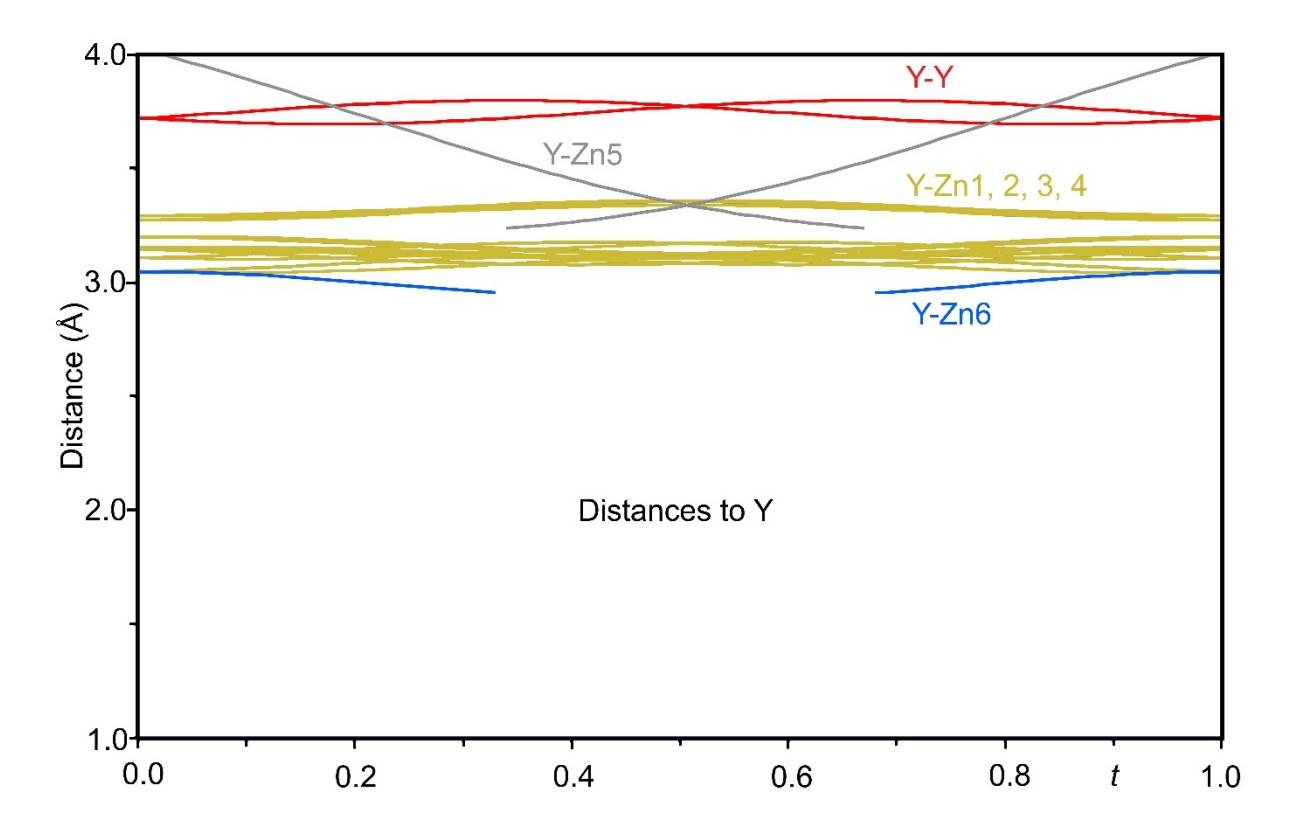
Table S2 WDS composition for different points and grains in the sample corresponding to YZn_{5+x} .

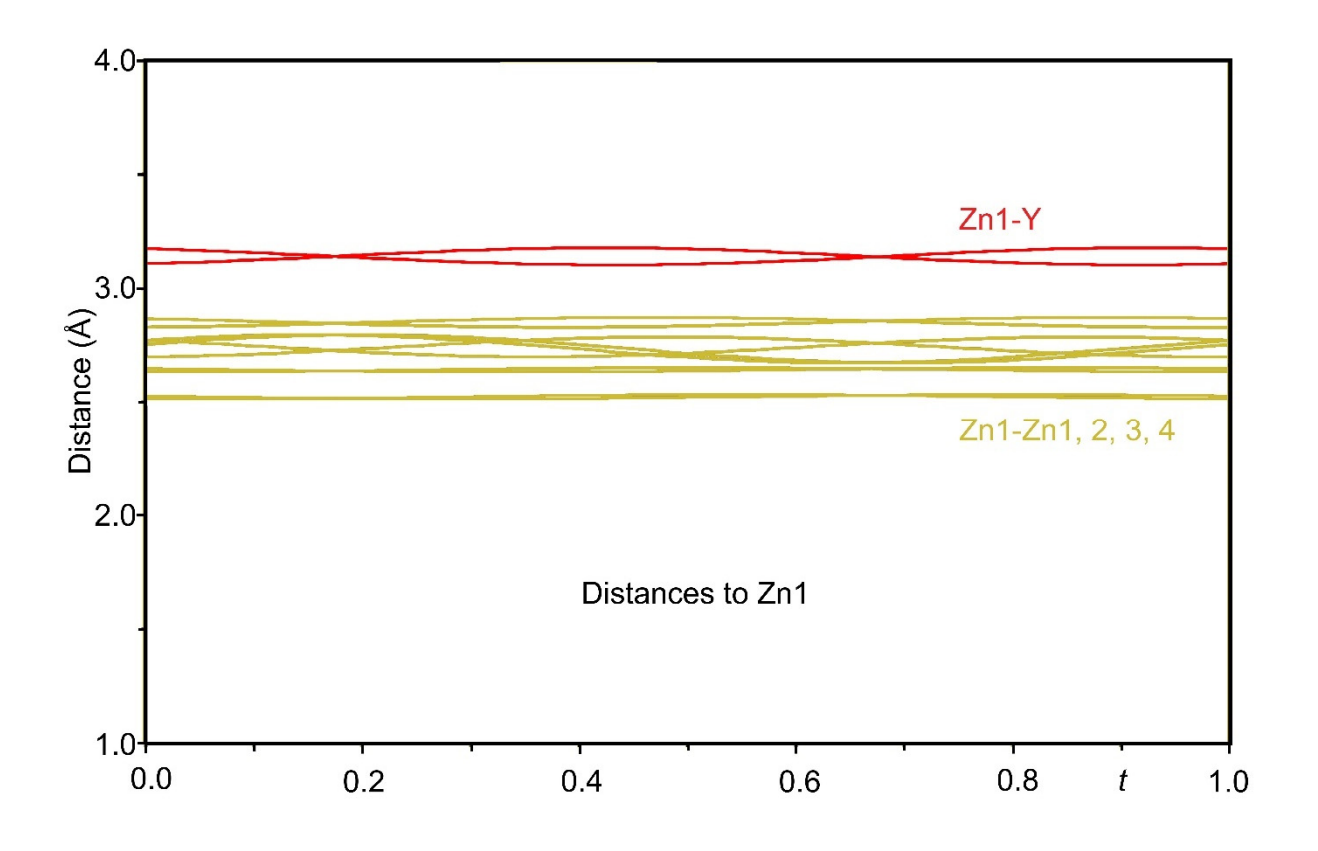
	LINE				
SAMPLE	No.	Y AT%	Zn AT%	TOTAL	Zn/Y
pt1_grain1_brightBSE	85	16.1604	83.8396	100	5.187966
pt2_grain1_brightBSE	86	15.8964	84.1037	100	5.290739
pt3_grain1_brightBSE	87	15.6964	84.3036	100	5.370888
pt4_grain1_brightBSE	88	15.5378	84.4622	100	5.435918
pt5_grain1_brightBSE	89	15.4998	84.5002	100	5.451696
pt6_grain1_brightBSE	90	15.9108	84.0892	100	5.285039
pt7_grain1_brightBSE	91	15.8043	84.1957	100	5.327392
pt8_grain1_brightBSE	92	15.4566	84.5434	100	5.469728
pt9_grain2_brightBSE	101	15.5527	84.4473	100	5.429752
pt10_grain2_brightBSE	102	15.6593	84.3407	100	5.385981
pt11_grain2_brightBSE	103	15.6538	84.3462	100	5.388225
pt12_grain2_brightBSE	104	15.1953	84.8047	100	5.580982
pt13_grain2_brightBSE	105	15.4028	84.5972	100	5.492326
pt14_grain2_brightBSE	106	15.2985	84.7015	100	5.536589
pt15_grain2_brightBSE	107	15.3944	84.6056	100	5.495869
pt16_grain2_brightBSE	108	15.5266	84.4734	100	5.44056
pt17_grain2_brightBSE	109	15.3552	84.6448	100	5.512452
pt18_grain2_brightBSE	110	15.1264	84.8736	100	5.610958
pt19_grain3_brightBSE	116	16.1158	83.8842	100	5.205091
pt20_grain3_brightBSE	117	15.8624	84.1376	100	5.304216
pt21_grain3_brightBSE	118	16.2426	83.7574	100	5.15665
pt22_grain3_brightBSE	119	16.1863	83.8137	100	5.178064
pt23_grain3_brightBSE	120	15.9442	84.0558	100	5.271873
pt24_grain3_brightBSE	121	16.5746	83.4254	100	5.033328
pt25_grain3_brightBSE	122	16.152	83.848	100	5.191184
pt26_grain3_brightBSE	123	16.0078	83.9922	100	5.246955
pt27_grain3_brightBSE	124	16.2611	83.7389	100	5.149645
pt28_grain3_brightBSE	125	16.5746	83.4254	100	5.033328
pt29_grain4_brightBSE	136	16.2954	83.7047	100	5.136707
pt30_grain4_brightBSE	137	16.2054	83.7946	100	5.170783
pt31_grain4_brightBSE	138	16.5179	83.4821	100	5.054038
pt32_grain4_brightBSE	139	16.5504	83.4496	100	5.04215
pt33_grain4_brightBSE	140	16.337	83.663	100	5.121075
pt34_grain4_brightBSE	141	16.0835	83.9165	100	5.217552
pt35 grain4 brightBSE					
pt55_grain4_brightb5E	142	16.2541	83.7459	100	5.152294

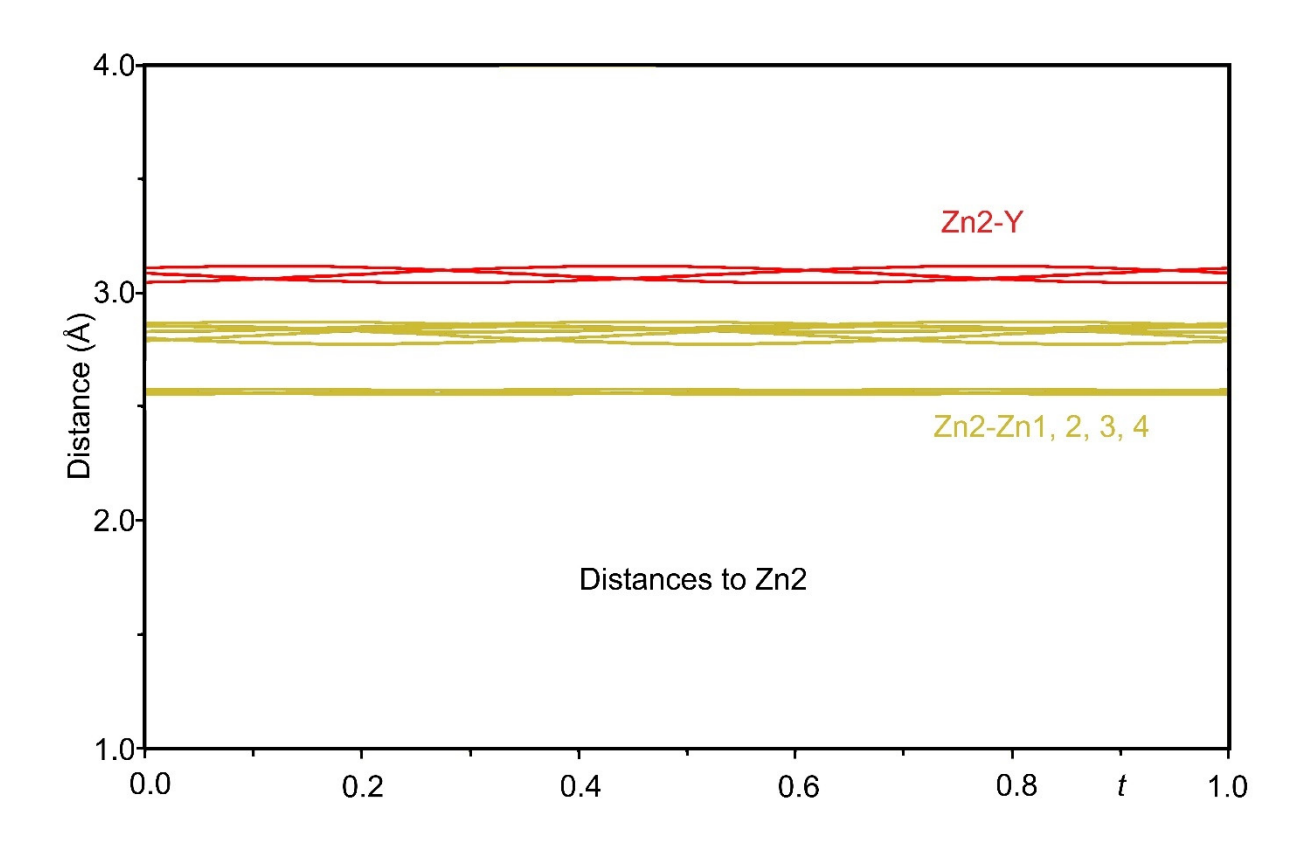
pt37_grain4_brightBSE	144	16.2074	83.7926	100	5.170021
pt38_grain4_brightBSE	145	16.3884	83.6117	100	5.101883
pt39_grain4_brightBSE	156	16.5491	83.4509	100	5.042625
pt40_grain4_brightBSE	157	16.6303	83.3698	100	5.013127
pt41_grain4_brightBSE	158	16.1005	83.8995	100	5.210987
pt42_grain4_brightBSE	159	16.6497	83.3503	100	5.006114
pt43_grain4_brightBSE	160	16.4717	83.5284	100	5.071025
Average of 43 points		15.97959	84.02042		5.262554
Standard deviation		0.435342	0.435332		0.171816
	·	· ·	· ·	·	

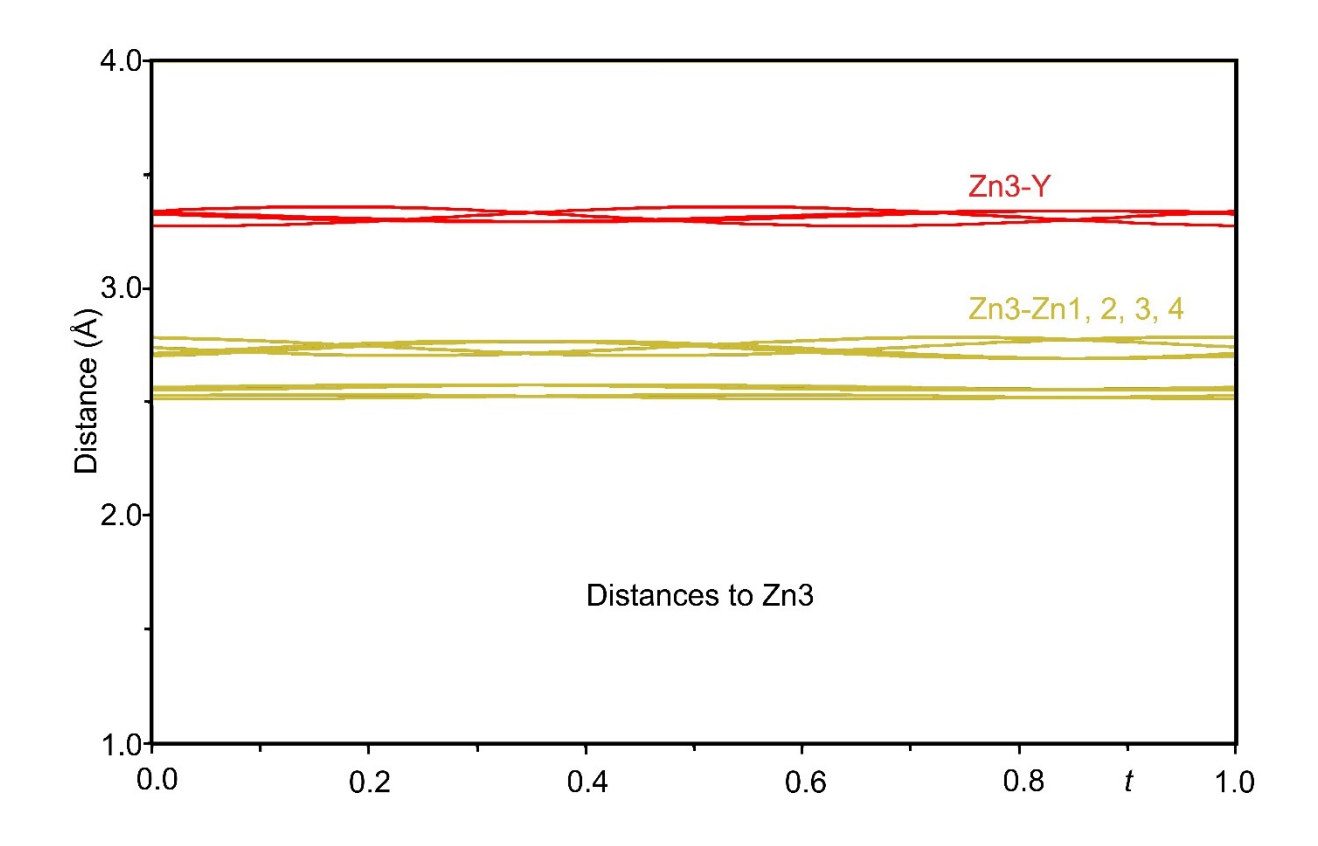
S4. Plots of crystallographic information for YZn_{5+x}

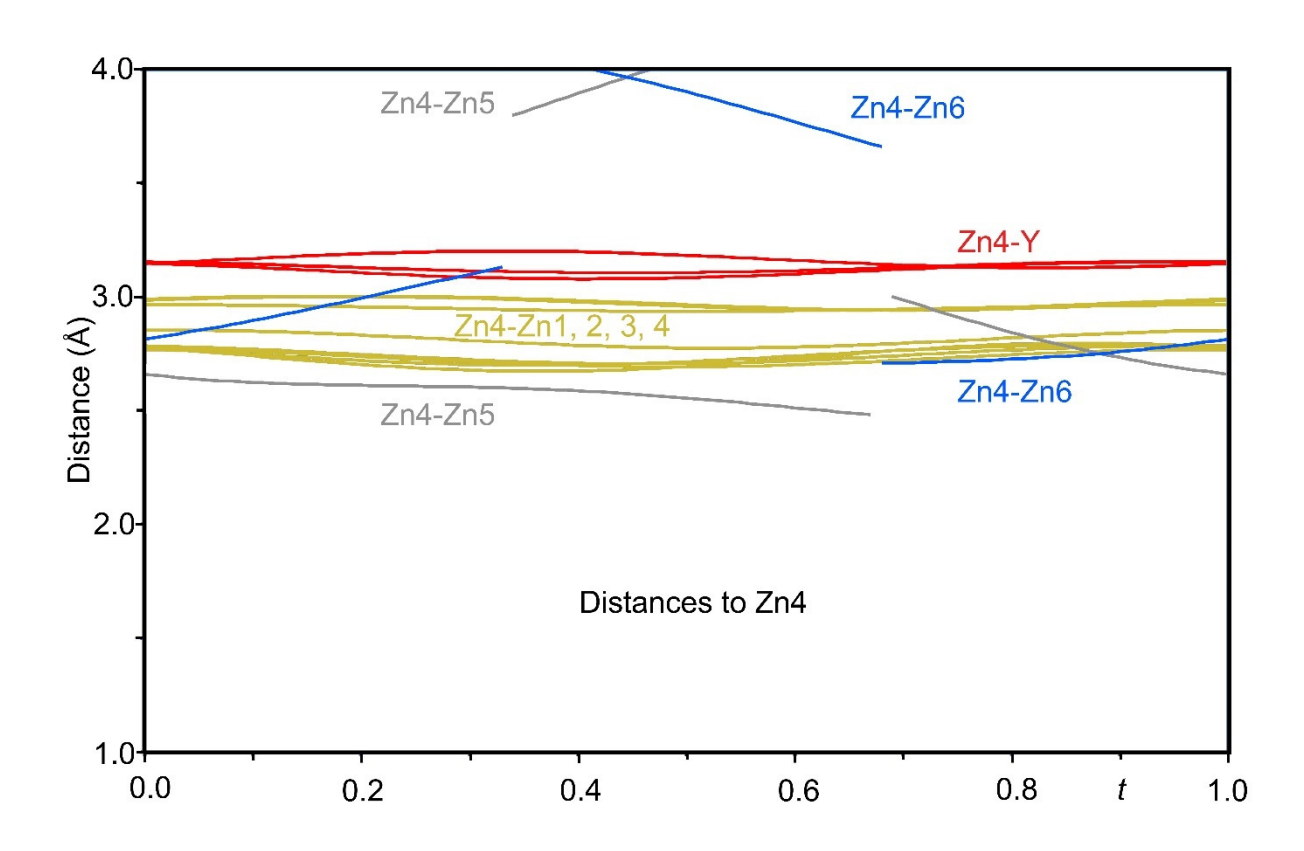
Figure S1 Interatomic distances of incommensurately modulated YZn_{5+x}

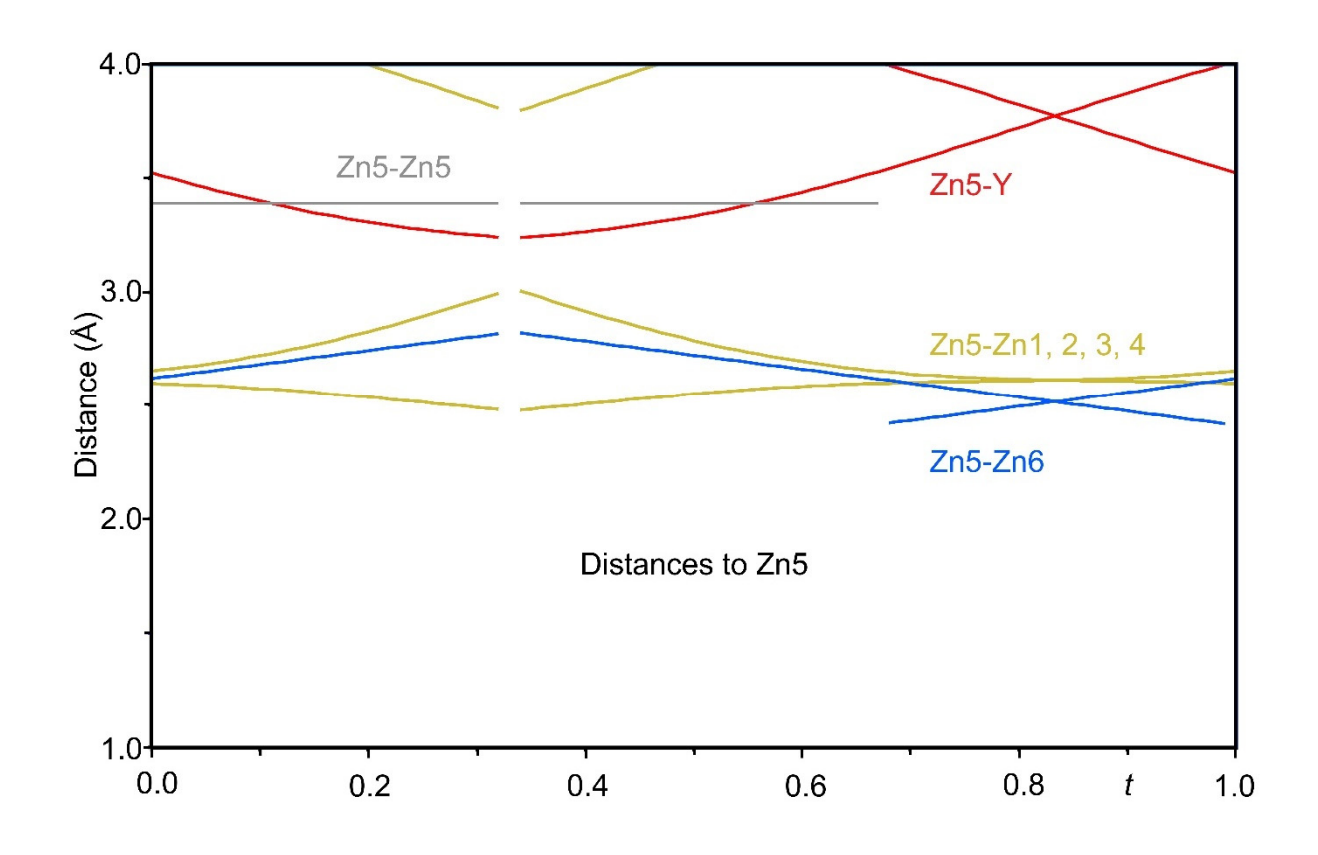












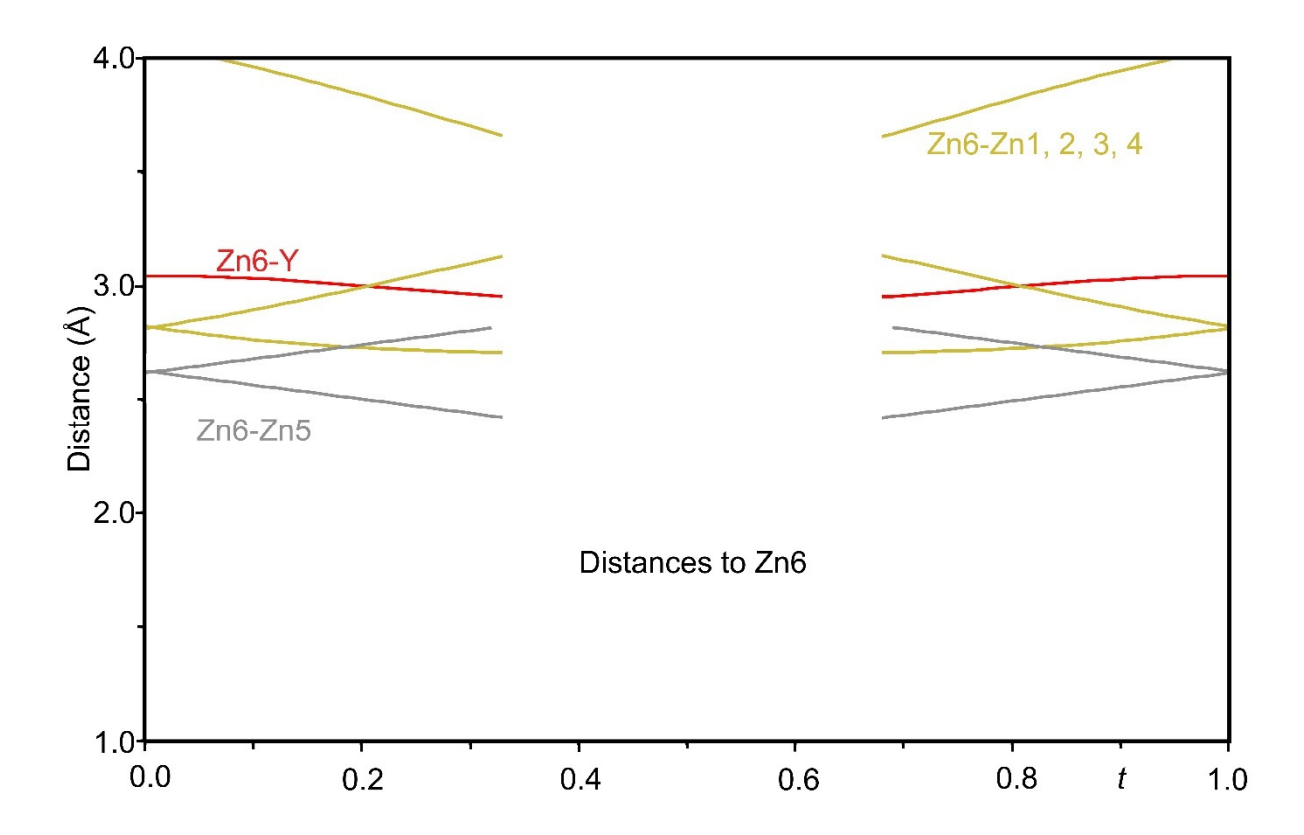
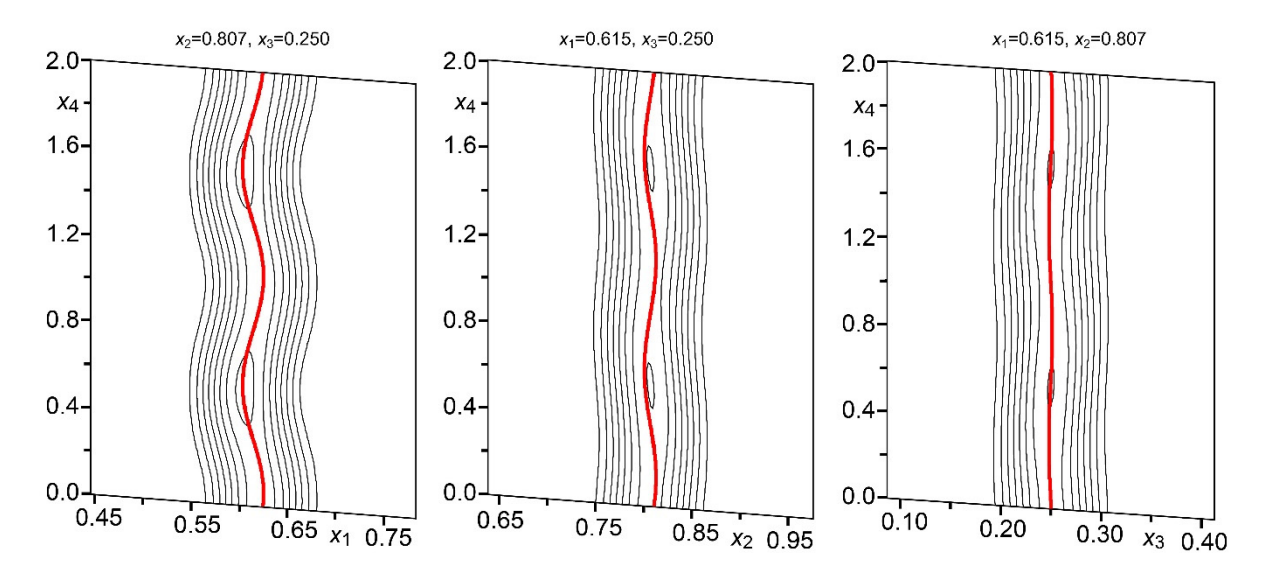
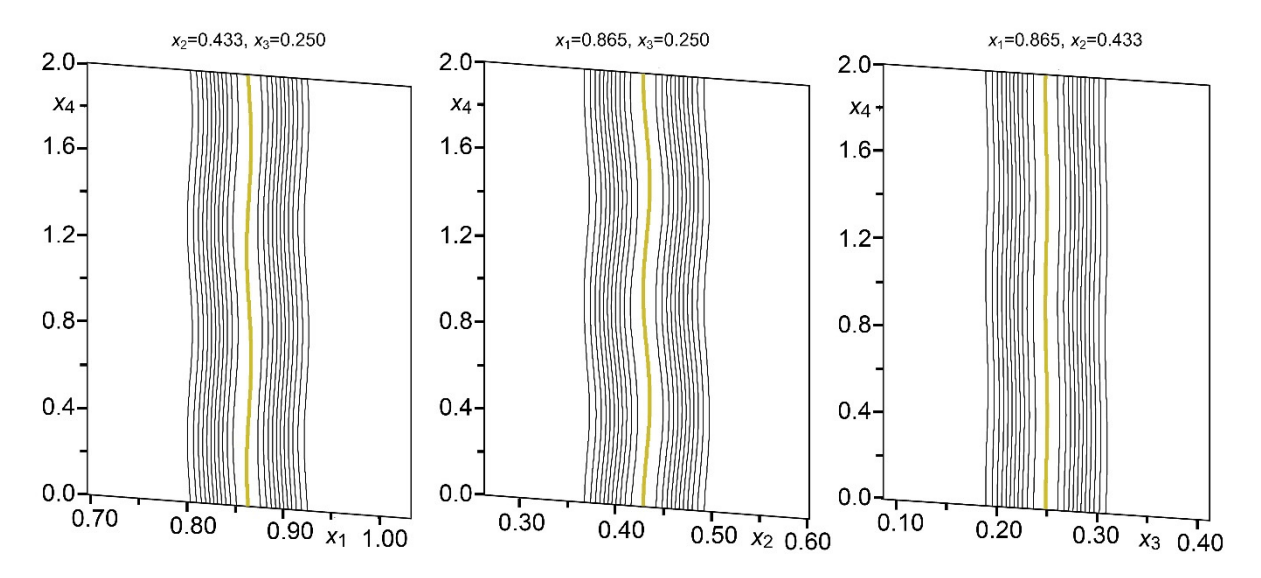
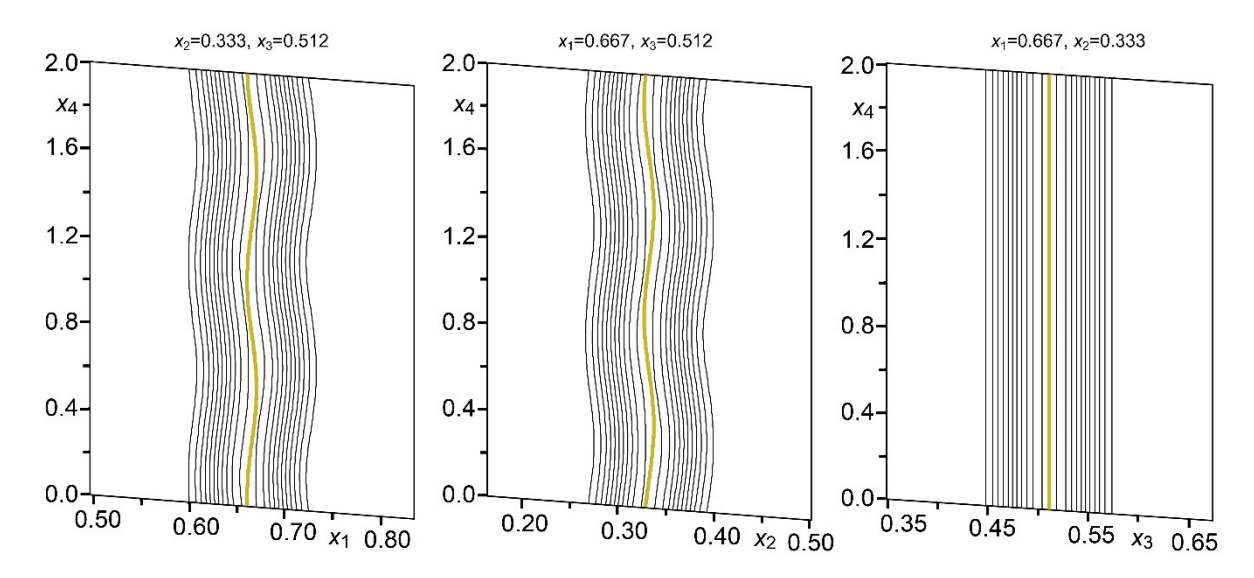


Figure S2 Observed Fourier electron density map cross sections centered on atomic positions in YZn_{5+x} .

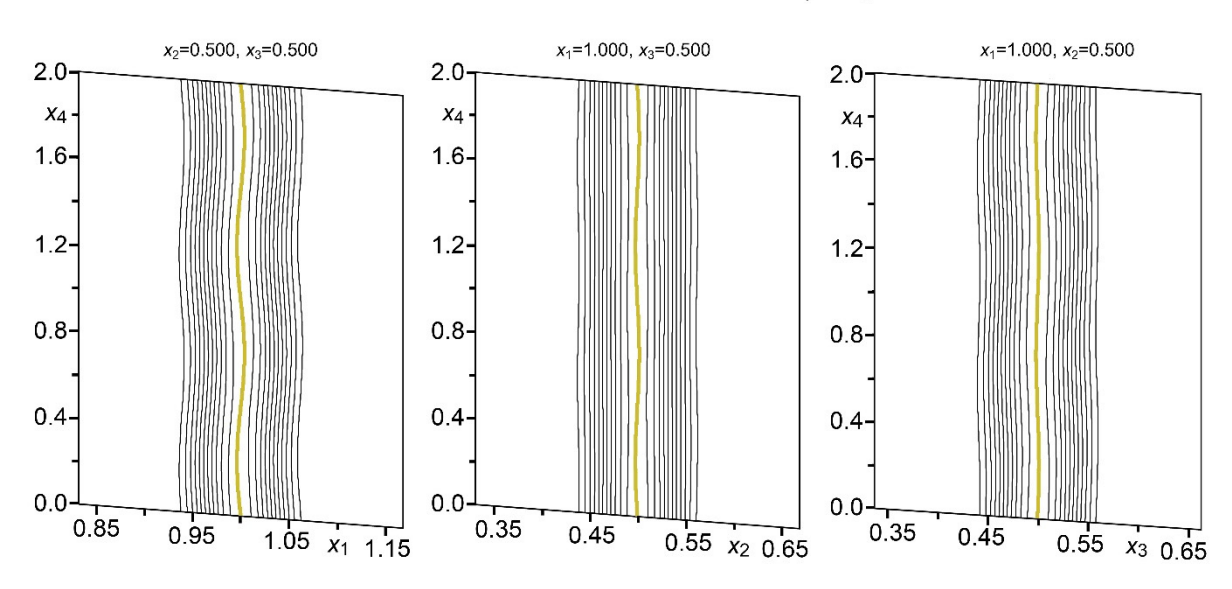
Cross sections of observed Fourier electron density map centered on Y



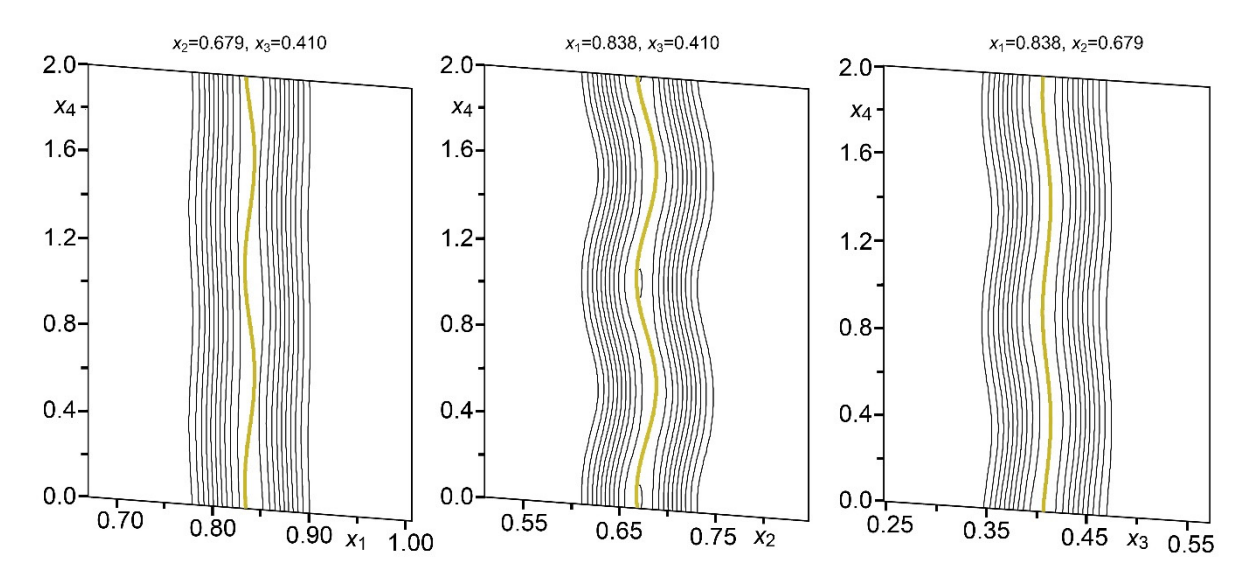


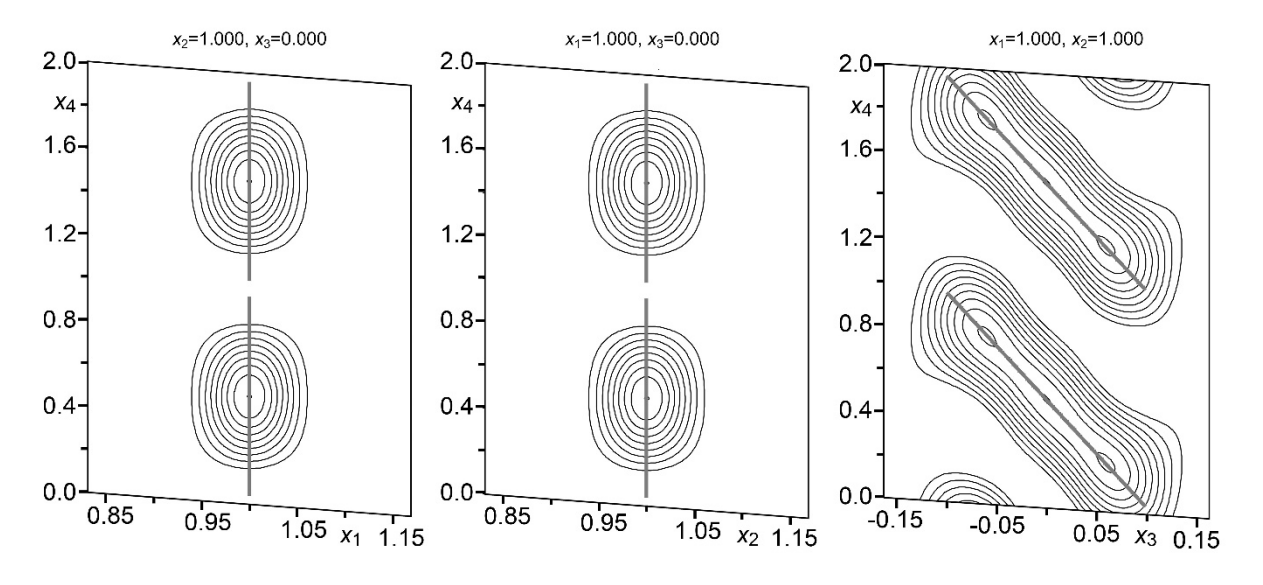


Cross sections of observed Fourier electron density map centered on Zn3



Cross sections of observed Fourier electron density map centered on Zn4





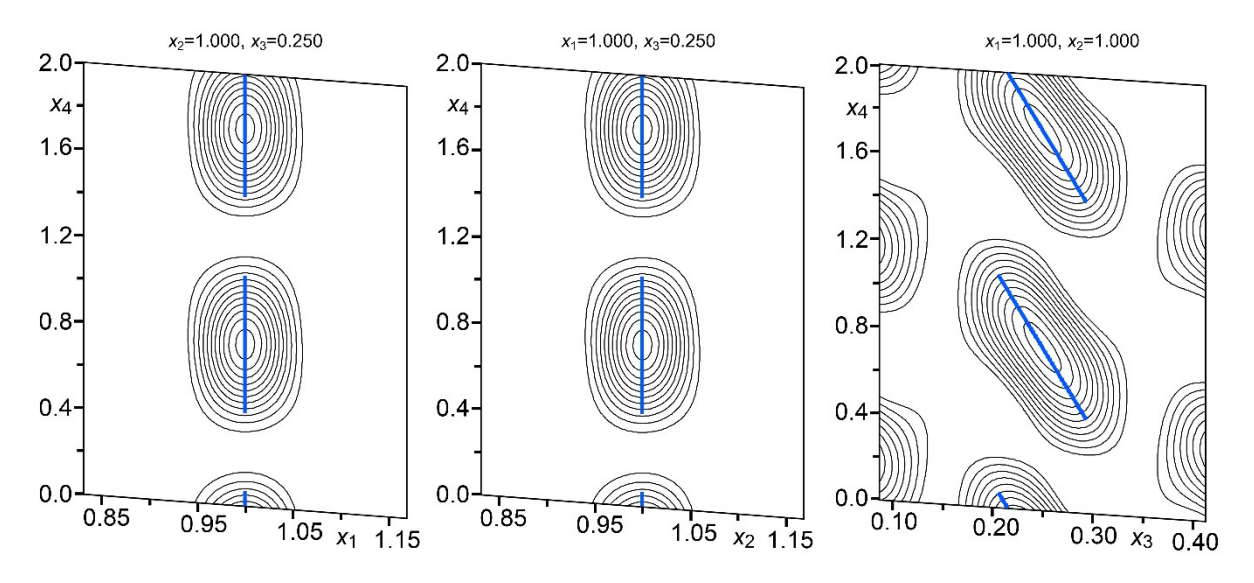


Figure S3 Examples of the YZn_{5+x} grains analyzed by EPMA. The lighter phase corresponds to YZn_{5+x} phase. (a) Line No. 86-92 (b) No. 136-140 in the lighter phase were used for WDS elemental analysis.

(a)

